Stony Brook University

A Model of the Mechanical Behavior of Vertically Aligned Carbon Nanotubes under Compression

A Dissertation Presented

by

Jian Yao

to

The Graduate School

in Partial Fulfillment of the

Requirements

for the Degree of

Doctor of Philosophy

in

Mechanical Engineering

Stony Brook University

May 2012

Stony Brook University

The Graduate School

Jian Yao

We, the dissertation committee for the above candidate for the

Doctor of Philosophy degree, hereby recommend

acceptance of this dissertation.

Dr. Robert Kukta - Dissertation Advisor
Associate Professor, Department of Mechanical Engineering

Dr. Chad Korach - Chairperson of Defense
Assistant Professor, Department of Mechanical Engineering

Dr. Imin Kao - Committee Member
Professor, Department of Mechanical Engineering

Dr. Gary Halada - Committee Member
Associate Professor, Department of Materials Science and Engineering

This dissertation is accepted by the Graduate School

Charles Taber
Interim Dean of the Graduate School

Abstract of the Dissertation

A Model of the Mechanical Behavior of Vertically Aligned Carbon Nanotubes under Compression

by

Jian Yao

Doctor of Philosophy

in

Mechanical Engineering

Stony Brook University

2012

A carbon nanotube (CNT) turf is composed of an array of nominally parallel aligned nanotubes that are weakly bonded together by van der Waals (vdW) forces. The structure is very compliant in compression and tends to deform by a unique buckling mechanism whereby small-wavelength buckles form and collapse in sequence. Subsequent buckles form adjacent to the previous buckle such that the deformation propagates across the loading axis of the specimen. The deformation appears as a propagating front that separates a distinct unbuckled region from a region consisting of a regular array of small-wavelength buckles. This behavior is quite different from that of a single CNT which would exhibit beam-like buckling. An axial supported beam undergoes large-wavelength buckling, which implies that the buckle wavelength is determined by the size of the structure (length of the beam). Undoubtedly, the added constraint associated with interactions between nanotubes affects the characteristics of the deformation in CNT turfs.

The purpose of this work is to propose a possible mechanism for the buckling behavior and test it with a mechanical model and computer simulations.

From stress versus strain measurements during compression, a CNT turf exhibits clearly different loading and unloading paths that indicate energy dissipation. The dissipation may be the result of a microstructural transformation such as debonding/rebonding of tubes or due to internal friction that occurs as tubes slide relative to each other within the potential field of van der Waals interactions. This work will assess the role of internal friction in the deformation process and determine if it might lead to the observed deformation mechanism of buckle formation and propagation. For this analysis, internal friction is treated as viscous force on a CNT as it deforms through an effective medium which accounts for the interaction of a nanotube with surrounding tubes. Finite element analysis is used to calculate results of the model.

It is found that the model exhibits progressive buckle formation from one end to the other end of the structure. The buckles form at a uniform size and propagate at a steady rate, which depend on the rate of compression. It is also found that buckling propagation occurs at a constant load such that the stress versus strain curve exhibits a distinct plateau. Buckle wavelength, plateau load and buckle forming rate are obtained as functions of the rate of compression, the bending stiffness of a nanotube and the viscosity of the effective medium. The bending stiffness characterizes elastic behavior of individual tubes in the turf and effective viscosity characterizes both the Vdw force between tubes and the density of tubes in the turf. The influences of nanotube geometry and material parameters on the deformation results are investigated.

Table of Contents

List of Figures

List of Tables

Acknowledgments

I am grateful for the guidance and encouragement of my advisor Professor Robert V. Kukta. His creative enthusiasm and broad knowledge in engineering and science will benefit me in my future careers. Besides my advisor, I would like to thank the rest of my dissertation committee, Professor Chad Korach, Professor Imin Kao and Professor Gary Halada, who gave insightful comments on my work. Last, but not the least, I would like to express my gratitude to my parents and my sister who give unconditional support and encouragement throughout my entire life.

Chapter 1 Introduction

1.1 Background

Carbon nanotube turfs possess numerous advantageous properties including low density, high strength, super elasticity at large deformations, good flexible resistance, good fatigue and fracture resistance. Consequently, they have been proposed for many applications, such as (1) for good fatigue resistant devices, accommodating high strain at over half a million cycles without fatigue failure [1], (2) as the inter layer fillings for energy-absorbing composites [2], (3) as a component to improve the fastening of connections between the adjacent plies in the 3D composite [3], (4) as the tunable membrane filter to allow the passing of certain sized particles depending on the compression pressure [4], (5) as nonlinear springs for energy absorption [5], and (6) as nanofoams with tunable and damping properties [6, 7]. The functions and performances are closely related to the porous structure. These functions are undoubtedly related with the nanoturf's structure.

Nanotube turf is an extremely complex porous and bundle-like structure composed of a large quantity of nearly vertically aligned, free standing nanotube arrays bonded by van der Waals interactions. The nanotube growing process is affected by van der Waals forces that cause cross links to form and provide structural integrity to the material. With increasing length, the nanotubes start to aggregate into bundles due to the unbalanced attractions from the neighbor tubes. The microstructure of nanoturf is characterized by active "pores" (disconnections between tubes) which can form and close depending upon adjacent nanotube positions and the entanglement of cross links. These geometrical and mechanical attributes make each nanotube in

the nanoturf deform much differently than an isolated nanotube. The mechanical properties of vertically aligned nanotube turf, such as deformation mechanism and macroscopic constitutive properties, are determined by the microscale behavior and understanding the microscale behavior is a key for the effective design and utilization of this material.

As many nanoturf applications involve cyclic compression loading and unloading, uniaxial compression measurements provide valuable engineering data. During compression of nanotube turfs, Cao et al. [7] found that small buckles form and collapse in a localized region near one end of the specimen. With increased deformation, the front of the buckled region propagates across the specimen in the axial direction of loading.

In summary experimental observations of turf deformation under compression have revealed many details of the mechanical behavior which have not yet to be fully explained.

1. Nanotubes deform by localized buckling wherein buckles propagate axially in sequence from one end to the other end of the specimen. This results in two distinct regions, a region with multiple small-wavelength buckles that accommodates most of the deformation and a region that is largely undeformed where the tubes remain nominal straight.
2. Buckle sizes are small compared to the specimen length and hence deformation does not follow simple Euler mode of buckling.
3. The buckles are of similar size.
4. During buckle formation the compression load exhibits a nearly constant plateau.
5. During each loading and unloading cycle a hysteresis loading curve is followed. After a certain priming period through which the hysteresis curve changes with each cycle, it saturates such that the same curve is traced for all subsequent cycles. This implies that all inelastic deformation (if any occurs) is completely recovered.

1.2 Motivation

Deformation occurs with small-wavelength buckles. It is known that buckle wavelength can be controlled through lateral confinement of a beam. For example the buckling of a beam glued to an elastic foundation will deform under compression as periodic waves or wrinkles rather than as a single large buckle. Stiffer confinement results in smaller buckle sizes [8]. If the confining force vanishes, the whole beam would buckle to form a single wave of maximum size. This understanding suggests lateral confinement from adjacent tubes may be responsible for finite sized buckling in a turf, but that alone does not explain the propagation of buckles. Propagation would also require that the degree of confinement is initially nonuniform and confinement changes ahead of the buckled region. It has been suggested that the density of tubes and hence degree of confinement might vary across a turf [9]. While tube density (and confinement) clearly increases within the buckled region, it is difficult to argue that it would increase significantly ahead of the buckles. Nevertheless, the constraint associated with interactions between nanotubes likely has an important role on the deformation mechanism [10]. It is noted that nanotubes in a turf contain very small wavelength intrinsic undulations. These are much smaller than the size of the buckles that arise from deformation. While these small undulation will likely have a role in activating buckle formation, it is unlikely that they directly determine the size of the buckles.

The hysteresis of the load-displacement curve implies there is energy dissipation during deformation. Furthermore it has been observed that higher compression rates result in a generally higher load [9]. Accordingly, it is reasonable to conclude that the interaction between nanotubes is largely viscous, or at least that a viscous interaction plays an important role in the deformation process. The viscous interaction will also confine tubes against buckling, albeit the

confinement will be time dependent. While it is quite likely that viscous effects alone do not completely explain the turf behavior, it is a valuable exercise to limit attention to viscous effect to determine what it might contribute to the behavior. Hence, a model is developed whereby the interaction between the nanotubes is treated as the viscous force, that is, the confined force against transverse motions of a tube is proportional to the transverse velocity of the tube. According to this model, the response of turf is determined by a viscous coefficient, the bending stiffness of a tube and the rate of compression. Outputs of the model that are of interest include that of plateau load, buckle propagation rate, and buckle size.

In the present work, a nanotube is treated as Euler beam under large deformations and calculations are made using finite element analysis. Dimensional analysis of the model is used to test the calculation and to limit the parameter space of the problem. It is noted that molecular dynamics method (MD) are often used to model nanotube deformations [11]. Although MD is suitable for some problems, it does require expensive computing resources and can be very time consuming for moderately large amounts of atoms. As tubes lengths of millimeters are required for this current problem, MD would be limiting. Furthermore, macroscopic deformations of a nanotube does not require full resolution of nanometer scale displacements and long tubes are well approximated as Euler beams [12].

There have been numerous recent experiments and qualitative analyses on the compressive behavior of nanotube turfs. Strain rate effect on the nanotube foam was explored [13]. Compression and indentation experiments were done on nanotube brushes to explore the buckling behavior [14]. Viscoelastic creep behavior was observed during indentation of vertically aligned nanotubes [15]. In situ testing revealed periodic buckle nucleation and propagation in nanotube bundles [9]. Height independency on compressive modulus of vertically

aligned carbon nanotube arrays was found and a simplified formula was used to discuss the buckle wave length [16]. The critical load was found depending on the total length [17]. A phenomenological mathematical formula was created for the nanofoam mechanical response [18]. The above analytical works are only based on the experimental observations and do not explain the mechanism that give rise to the deformation behavior; they assume the behavior occurs and analyze the consequences. The goal of this work is to provide insight on what causes the fundamental behavior.

1.3 Objective

The investigation develops on the proposed understanding of nanotube buckle evolving mechanism using the static model of nonlinear beam bending under lateral viscous surface load in two dimensional plane. In accordance with the experimental observation it is expected equal sized self folding will be found progressing from one end to the other end at constant plateau load on the displacement controlled loading condition. Quantitatively the buckle forming rate, buckle length and buckle plateau load are to be verified to conform to the formulas in terms of the bending stiffness, viscosity and compression rate from dimensional analysis. The parameters of beam total height, perturbed geometry variations and cross area stiffness are to be checked for their influences on the deformation results.

1.4 Dissertation Structure

This dissertation is organized as follows. Chapter 2 provides an introduction to carbon nanotube turfs structure and deformation mechanism and presents the mechanics model used to further simulate the deformation behavior. The growth process and the resulting microstructure

are discussed first, followed by a discussion of the buckling deformation mechanism and related experimental work and measurements. The model is then presented and the governing equation for the deformation of a nanotube is derived. In Chapter 3, the governing equation is cast into a weak form suitable for finite element analysis. This form determines the proper application of nodal forces and moments to represent the distributed time-dependent viscous load. Additionally it determines the corresponding stiffness of these nodal loads as is required for time-stepping. In Chapter 4, simulations of the single beam progressive buckling are conducted. The formulas for plateau load, buckle forming rate, and buckle wave length are derived from the dimensional analysis. In addition investigations on the perturbation effects and effects of beam area stiffness and total height on the buckle results are conducted. Chapter 5 gives the conclusions based on the present work.

Chapter 2 Structure, Mechanics and Modeling of Carbon Nanotube Turfs

Motivated by compression test observations [7], the current study is done to provide insight to the deformation behavior of nanotube turfs using a model for the nanotube buckling under a viscous lateral confinement. Specifically, the goal is to determine how the viscous confinement affects nanotube buckling under large deformations. This section provides some background on the structure and deformation of nanotube turfs in order to motivate the model and some explanation on the simplification of structure internal interaction into the viscous friction. The model, developed in context of continuum Euler beam theory, is then presented and the governing differential equation of nanotube deformation is derived.

2.1 Nanoturf Structure

Nanotubes in a turf tend to form the bundles as shown in Figure 1a. This bundling is driven by attractive van der Waals interaction between tubes, which is a fairly short ranged interaction. In order for bundling to occur, tubes in a turf must bend towards each other and, hence, bending energy provides a penalty against bundling. Bending energy is long ranged; tubes that are constrained at one more sites, must deform to enter the bundles and the deformation (and hence the bending energy) grows as the distance from constrained sites becomes further from the bundle. The competition between adhesive energy (van der Waals) and bending energy establishes a length scale for the degree of bundling that can occur in a turf. Instead of all the tubes forming into one big bundle, the structure is rather porous as shown in Figure 1a.

Compared with the shorter tubes (~100nm) of Figure 1a, the longer tubes become wavy along the axial direction (Figure 1b).

Nanotubes in a turf have a range of diameters due to local variations in catalytic gas feeding rate. The growth rate of CNTs of larger diameters is slower than that of smaller diameters because more carbon atoms are required to form a thicker tube of the same height [19]. Van der Waals forces between the neighboring nanotubes help to maintain the top surface at uniform turf height, as the smaller diameter softer CNTs become bent to match the height of larger diameter stiffer CNTs [19]. The competition of nanotubes stiffness that supports adjacent vdW attractions and internal bending moments results in the presence of periodic wave for each nanotube [19]. Thus ripples form spontaneously during growth. This hypothesis is consistent with Figure 1b and c, where CNTs of different bending degrees can be clearly observed. Because of high stiffness the height of large diameters nanotubes determines the forest height [19]. The random arrangement of CNTs ensures a continuous distribution of the porosity, maintaining a homogenized structure. The wavelength of these small grown-in wavy patterns is fairly uniform throughout the structure. Uniform van der Waals force occurring in the homogenized structure leads to the fairly equal sized wavelength. It is noted that wavelength of these ripples is over an order of magnitude smaller than that of the deformation induced buckles discussed next. The tubes are in the cohesive state.

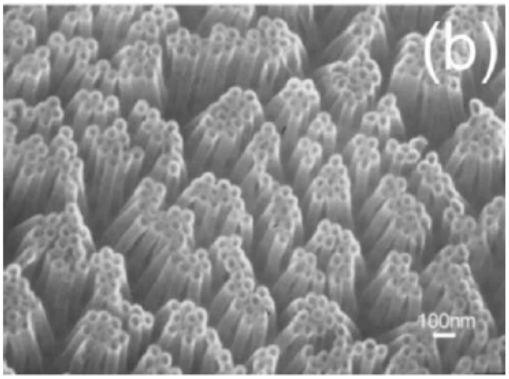

(a)

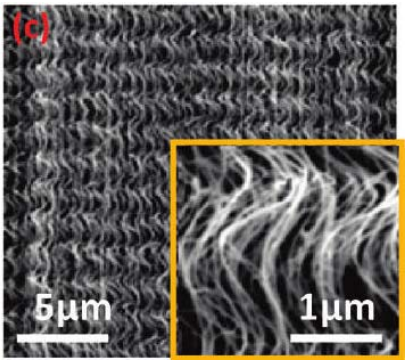

(b)

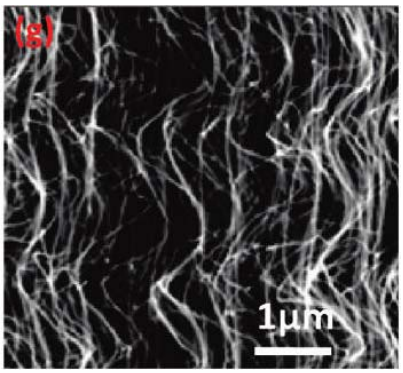

(c)

Figure 1 Nanoturf microstructure. (a) Nanotubes of ~100nm length are attracted each other by vdW force, and gaps between bundles are existing [20]. (b) Compressive strain regulates nanotubes as periodic waves [19]. (c) Magnified image of (b) indicating changing curvatures of CNTs in the nanoturf. Longer nanotubes of ~1μm length presenting the serpentine shape and displaying larger lateral bending displacements resulted from the vdW force [19].

2.2 Mechanics of Nanotube Surface Load

Uniaxial compression loading and unloading of vertically aligned nanotubes arrays were studied by Cao et al. [7]. They subjected the specimens to repeated loading cycles and found that after thousand cycles the cycle curve becomes saturated indicating no residual (macroscopic) deformation upon unloading. Repeated loadings after unloading follow the same route, that is, every time after unloading nanoturf regains the same stiffness. It means the fracture doesn't occur along each nanotube axis. While the loading/unloading curve exhibits a hysteresis. Energy is lost during the loading/unloading cycle while the deformation is fully recovered. As this behavior is repeatable, it is most likely the result of internal viscous dissipation. Generally the viscous force is resulted from the relative movement between the adjacent materials. Specifically this viscous energy dissipation is resulted from the different nanotubes impacting rater than the single nanotube fracturing.

As to investigate the mechanism which leads to localized buckles, exploration starts by considering the relative movement of neighboring nanotubes in deforming structure. Figure 3 (a) shows the structure consisting of vertically aligned and homogeneously positioned nanotubes with equal height. Figure 3 (b) shows the random nanotube deformations under uniform axial compression. Boundary conditions specify that at top ends transverse displacements are fixed and vertical velocity remains same at top end for every nanotube. Under longitudinal compression nanotubes resist each other to form the friction by opposite bending in the transverse direction. Because of equal friction on both sides resulted from a same transverse distance in the initial homogeneous structure and of equal bending stiffness for each nanotube lateral bending of each nanotube to either side occurs to the same extent. Further bending develops on the basis of previously deformed homogeneous structure and nanotubes

deformations do not vary with locations. Figure 3 (c) shows one pair of nanotubes deforming against each other. S_1, S_2, θ_1, θ_2, V_1, V_2, F_1, F_2, α_1, α_2 are natural coordinates along longitudinal directions, beam orientation angles at top ends, velocity vectors, friction forces, and velocity directions respectively for nanotubes of #1 and #2. From above discussion due to the same level bending deformation these two nanotubes always form the symmetrical shape such that $\theta_1=\theta_2$, $\alpha_1=\alpha_2$, $V_{1x}=V_{2x}$, $V_{1y}=V_{2y}$. Thus for any pair of contacting nanotubes the relative movement only occurs transversely. Hence generated friction force F_1 and F_2 are along transverse direction.

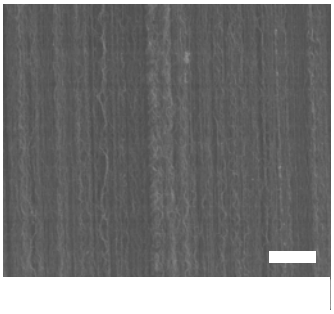

(a)

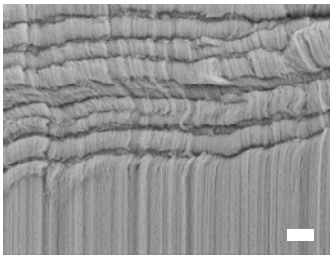

(b)

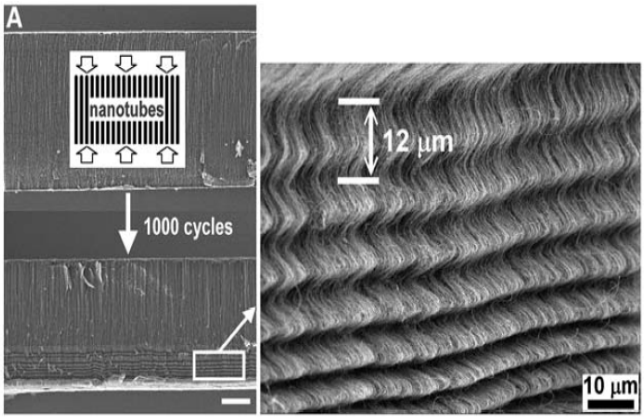

(c)

Figure 2 Nanoturf containing free standing vertically aligned nanotubes of same height is compressed in thickness direction and shows special behavior. (a) Photo of uncompressed as grown CNTs indicates all nanotubes are not purely straight (5 μm scale bar) [21]; (b) After application of uniform compression on top surface, the transition interface between deformed portion and undeformed portion is shown in the middle part (10 μm scale bar) [21]; (c) As uniform compression applies on the top surface, the horizontally uniform buckles of similar size evolve from the bottom end progressively and coordinately [7].

To illustrate the friction force magnitude, the discussion focuses on the effective amount of nanotubes swept by unit length nanotube. In the 2D plane every nanotube is surrounded by the neighboring large quantities of nanotubes such that at any deformation position this nanotube does not stay out of the grey region as shown in Figure 3 (d). When moving transversely at distance S, nanotube must sweep through neighboring nanotubes which lie in the parallelogram blank region (Figure 3 (d)). Within unit time increment larger blank area results in sweeping of more nanotubes which requires increased force to balance the increased resistance ascribed to more contacts with neighboring nanotubes. The compression force might be constant or non-constant relying on the compression rate. Hutchens et al. [9] found the compression stress has a strong dependence on the strain rate. Hence, it is natural to expect an increase in the resistance magnitude with an increasing deflection velocity. In Figure 3 (d) initial surrounding area is homogenized, and after nanotube transverse movement the area homogeneous density is destroyed. The vicinity nanotubes require long time to relax and yield enough space for the insertion of new nanotube to the limited space. As going through same transverse distance with less time, it leads to the higher local density gradient which cannot relax in a short time and form a larger resistant force. From previous discussion the neighboring nanotubes do not have relative vertical motion thus only global transverse velocity is considered effective for sweeping area. The lateral resistance is such that the complete vector for resistance force is defined as

$$F_x = -K \cdot v_x \cdot \sin\theta \tag{2-1}$$

F_x is proportional to quantity of affected neighboring nanotubes by the moving nanotube of transverse distance on unit time. The resistant force magnitude is defined by the instant velocity and orientation at the current location. It can be observed that the horizontal oriented penetrating nanotube experiences the zero resistance for zero affected area, while the vertical oriented

punching motion experiences the maximum resistance for maximum affected area. The viscous force is applied on the beam surface referred as surface load. Since the nanoturf is growing homogeneously, any location's density is similar to the other locations. Thus the viscosity K is set as constant throughout the whole structure. Note the F_x unit is F/L which means the F_x is the force density along the surface. This v_x (unit: L/T) is the global velocity projection on the fixed x direction that may change with the time. θ is the instant orientation of the unit surface measured along counterclockwise from the positive x axis. If θ less than zero, take absolute value of $Sin\theta$. Since this viscous force is functioning as resistance to the movement, the resistant force direction is always towards the opposite direction of the horizontal velocity. It is noted that the velocity projection on vertical direction does not have any influences on the viscous force magnitude, and the surface's orientation does have significant effect on the viscous force magnitude.

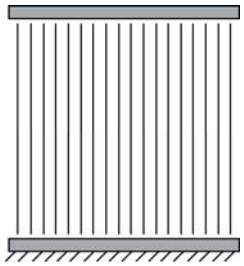

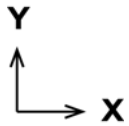

(a)

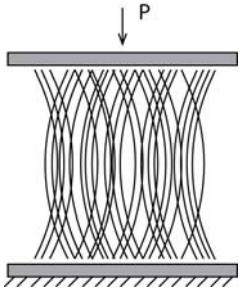

(b)

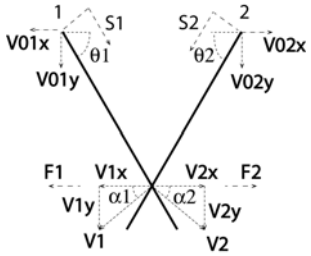

(c)

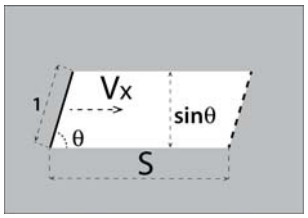

(d)

Figure 3 Schematic of the viscous force; Lines represent single nanotube; (a) structure of the undeformed nanoturf; (b) structure of the deformed nanoturf; (c) illustration of the friction force resulted from a pair of contacting nanotubes; (d) Gray colored area represent neighboring

nanotubes without affected, and blank area represents those affected.

2.3 Model of Nanotube's Large Deformation

The nanotube turf consists of numerous vertically aligned nanotubes. Each nanotube is modeled as two-dimensional large deformation Euler beam of isotropic linear elastic material with cross-section being same through whole length, neutral axis of which is perpendicular to the cross section at any deformation state implying that the cross section plane's normal is along the tangential direction of the beam neutral curve so that any cross section's deformation occurs by bending alone without any shear deformation. Beam bending stiffness is *EI*. Axially the beam is rigid and modeled as inextensible. *s* is the natural coordinate along the beam length direction. Here the *s* is defined as the natural coordinate along the beam starting from 1 and ending at 2 in Figure 5. On the beam surface exists distributed viscous force which is only in the global horizontal direction (Figure 5). Beam presents the bent shape under the applied concentrated forces *P*, *V* and the moment *M* at both ends and distributed viscous force (Figure 5).

Beam bending extent is defined by curvature which is largely dependent on normal and tangential vector. Tangential and normal vectors can be defined in terms of coordinates respectively as (Figure 4)

$$\vec{t} = \left\{ \frac{dx}{ds} \quad \frac{dy}{ds} \right\}^T \qquad \vec{n} = \left\{ \frac{dy}{ds} \quad -\frac{dx}{ds} \right\}^T \tag{2-2}$$

The above formulas are expressed in the parameter function with *s* as the independent variable. $\vec{n}$ and $\vec{t}$ are unit vectors orthogonal to each other. Note that on the 2D plane the normal vector $\vec{n}$ is always on the right hand side of the tangential vector $\vec{t}$ in the sense that they observe the right hand rule such that one can start from the $\vec{n}$ and stop at $\vec{t}$ within an right angle in the two

dimensional plane. Magnitude of Curvature describes bending extent, while sign of that describes bending direction. Curvature is defined as rate of change for tangential angle along beam length, that is, $\frac{d\theta}{ds}$. Mathematically curvature *k* is given as the normal vector $\vec{n}$'s change along the natural coordinate *s* in the direction of $\vec{t}$.

$$\kappa = \frac{d\vec{n}}{ds} \cdot \vec{t} \tag{2-3}$$

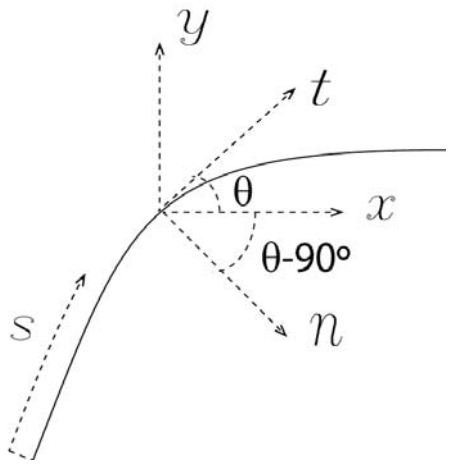

Figure 4 Illustration of curvature definition

$\vec{t}$ is along increasing direction of natural coordinate *s*, and it is a unit vector denoted as

$$\vec{t} = \cos\theta\vec{i} + \sin\theta\vec{j} \tag{2-4}$$

$\vec{n}$ is normal vector orthogonal to tangential vector, therefore direction angle is $\theta - 90^\circ$ as

$$\vec{n} = \cos(\theta - 90^\circ)\vec{i} + \sin(\theta - 90^\circ)\vec{j} \tag{2-5}$$

In fact (2-3) can be proved by following (2-4) and (2-5) normal vector change projection on $\vec{t}$'s direction is

$$\begin{aligned}\frac{d\vec{n}}{ds}\cdot\vec{t} &= \frac{d\theta}{ds}\left(\cos\theta\vec{i}+\sin\theta\vec{j}\right)\cdot\left(\cos\theta\vec{i}+\sin\theta\vec{j}\right)\\ &= \frac{d\theta}{ds}\\ &= \kappa\end{aligned} \tag{2-6}$$

In terms of Cartesian coordinate using (2-2) and (2-3) κ can be shown as

$$\kappa = \frac{d\vec{n}}{ds}\cdot\vec{t} = \frac{d^2y}{ds^2}\frac{dx}{ds} - \frac{d^2x}{ds^2}\frac{dy}{ds} \tag{2-7}$$

In Figure 5 *x* is the accumulation along the abscissa.

$$x = \int_0^s \cos\theta ds \tag{2-8}$$

$$\frac{dx}{ds} = \cos\theta \tag{2-9}$$

In Figure 5 *y* is the accumulation along the ordinate.

$$y = \int_0^s \sin\theta ds \tag{2-10}$$

$$\frac{dy}{ds} = \sin\theta \tag{2-11}$$

Accordingly,

$$\frac{d^2x}{ds^2} = \frac{d}{ds}\left(\cos\theta\right) = \frac{d}{d\theta}\left(\cos\theta\right)\frac{d\theta}{ds} = -\kappa\sin\theta \tag{2-12}$$

$$\frac{d^2y}{ds^2} = \frac{d}{ds}\left(\sin\theta\right) = \frac{d}{d\theta}\left(\sin\theta\right)\frac{d\theta}{ds} = \kappa\cos\theta \tag{2-13}$$

Above are the complete geometric conditions in order to define the two dimensional Euler beam deformations.

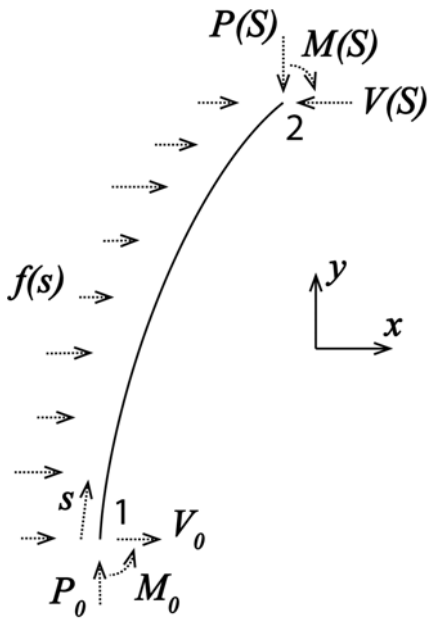

Figure 5 Schematic illustration for the deformed beam geometry

In bending process beam is accommodating vertical force *P*, lateral force *V*, moment *M* and lateral surface force *f* (Figure 5). Because in the *y* direction there is not any other external applied force along the beam except on both ends, along the whole beam *P* does not change which implies

$$P(s) = P_0 \tag{2-14}$$

P_0 is constant so that vertical force *P* is equal at any location in beam. *V* is reaction force of surface distributed force *f*, and is denoted as shear force along the abscissa following the same direction as distributed force. *V*'s change is equal to accumulation of surface forces along the beam. Therefore change of *V* is only dependent on the distributed load *f* such as

$$V(s) = V_0 + \int_0^s f(s)ds \tag{2-15}$$

Euler beam is a pure bending beam which does not allow shear deformation, so geometrically *M* is the reaction moment only resulted from beam curvature change as

$$M(s) = EI \cdot \kappa(s) \tag{2-16}$$

From mechanics, the moment is affected by all variables which have moment contributions along the beam length. Moment equilibrium at point 1 implies (Figure 5)

$$M_0 = M(S) + P(S)x(S) - V(S)y(S) + \int_0^S y(s)f(s)ds \tag{2-17}$$

In order to get equilibrium in differential form and remove the integral expression, combining (2-17) and using (2-16) $M=EI\cdot\kappa$, one may differentiate twice the above equation at both sides to get

$$EI\frac{d^2\kappa(S)}{dS^2} + P_0\frac{d^2x(S)}{dS^2} - V(S)\frac{d^2y(S)}{dS^2} - f(S)\frac{dy(S)}{dS} = 0 \tag{2-18}$$

This is a second order ordinary differential equation. P_0, V, f and κ are all dependent on coordinates x and y, and one needs to use nonlinear geometric iterative Newton-Rahpson scheme to solve this equation. The time rate effect is considered in the simulations. However because the nanotube mass is too small compared with the bending stiffness thus mass is not considered in the equilibrium equation which only includes the beam bending terms and the environmental viscous resistance so as to not involve the kinetic energy and to obtain more essential nanotube's buckling behavior under viscous effect, since buckling would be otherwise very sensitive to the mass incurred inertia and momentum. The fracture in nanotube is not considered in the simulation because the nanotube is extremely flexible and tough from experimental observations [7]. The nanotube is purely elastic continuum, and all the large deformation is resulted from the nonlinear geometry bending deformation since the beam is of linear elastic continuum solid.

Chapter 3 Numerical Implementations for Distributed Viscous Surface Load

In order to investigate effect of surface viscous load on nanotube buckle process by finite element method, the distributed viscous load must be formulated into the FEM form as the nodal force and nodal moment. The following section strictly observes the standard FEM procedure to give the explicit formulas of nodal forces and nodal forces' stiffness in terms of the nodal degrees of freedom and time change so that combined with beam stiffness and boundary conditions the global equilibrium equations can be readily formed.

3.1 Beam Element's Nodal Force

Energy conservation requires external work equal to beam's internal deformation energy. One can obtain beam element stiffness matrix from internal work, and external nodal force from the external work. In order to obtain the equivalent nodal forces resulted from distributed load only external work W_E done by surface distributed viscous load is considered in this work.

$$W_E = \int_0^L q \delta X ds \tag{3-1}$$

This integral implies that explicit expressions in terms of beam arc length s are needed for deformed shape X of a beam and surface load q on a beam. A method of evaluating X and q is obtained from constructing a continuous shape by interpreting function values and their derivatives at both ends.

Consider a general nonlinear large deformation two-dimensional Euler beam element. The displacement and coordinate (before and after deformation) of every point on the beam neutral

axis can be interpolated by the nodal degrees of freedom i.e. displacements and rotations. Here and elsewhere the displacements and coordinates are used only for point on the beam's neutral axis. In (2-7) the curvature is expressed in terms of coordinate derivatives at the first and second order. For the requirement of displacement, rotation and curvature to be continuous and smooth so that the minimum shape interpolation

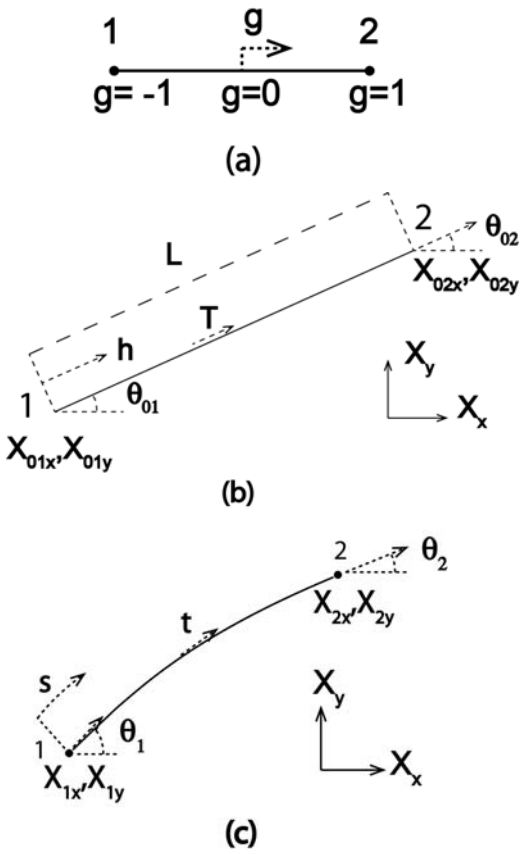

Figure 6 Illustration of Euler beam element. (a) Parameter element (b) Undeformed stress-free element (c) Deformed element

should be Hermitian polynomial functions. In order that the element is basically isoparametric, Hermitian polynomials are used to interpolate the components of both total global displacement u of any point along the beam neutral axis and initial position vector X_0 as [22]

$$u(g) = N_1(g)u_1 + N_2(g)u_2 + N_3(g)\frac{\partial u}{\partial g}\Big|_{g=-1} + N_4(g)\frac{\partial u}{\partial g}\Big|_{g=1}\ ,\ -1 \le g \le 1 \qquad (3\text{-}2)$$

$$X_0(g) = N_1(g)X_{01} + N_2(g)X_{02} + N_3(g)\frac{dX_0}{dg}\Big|_{g=-1} + N_4(g)\frac{dX_0}{dg}\Big|_{g=1}\ ,\ -1 \le g \le 1 \qquad (3\text{-}3)$$

where natural parameter $g = -1$ at node 1, $g = 1$ at node 2 and g = 0 at middle point as shown in Figure 6(a). N_1~N_4 are Hermitian polynomial shape functions shown by

$$N_1 = \frac{1}{4}(g^3 - 3g + 2) \qquad N_2 = \frac{1}{4}(-g^3 + 3g + 2)$$
$$N_3 = \frac{1}{4}(g^3 - g^2 - g + 1) \quad N_4 = \frac{1}{4}(g^3 + g^2 - g - 1) \qquad (3\text{-}4)$$

u and $\frac{\partial u}{\partial g}$, which are unknown variables resulted by deformation, are respectively nodal displacement and its derivative about parameter g. X_0 and $\frac{dX_0}{dg}$ are respectively undeformed initial coordinate and its change about the parameter g. Since both coordinate (before deformation) and displacement can be separately interpolated as Hermitian polynomials, then global position (after deformation) of any point on the beam element can be interpolated by the nodal values through Hermitian functions as

$$\begin{aligned} X &= X_0 + u \\ &= N_1(X_{01} + u_1) + N_2(X_{02} + u_2) + N_3\left(\frac{dX_0}{dg}\Big|_{g=-1} + \frac{\partial u}{\partial g}\Big|_{g=-1}\right) + N_4\left(\frac{dX_0}{dg}\Big|_{g=1} + \frac{\partial u}{\partial g}\Big|_{g=1}\right) \\ &= N_1X_1 + N_2X_2 + N_3\frac{\partial X}{\partial g}\Big|_{g=-1} + N_4\frac{\partial X}{\partial g}\Big|_{g=1} \end{aligned} \qquad (3\text{-}5)$$

where X_1 and X_2 are simply initial positions plus unknown translational displacements which are easy to acquire, but calculation of $\frac{\partial X}{\partial g}$ involves tangential vector in terms of rotation θ. Let t represent the tangential vector at any point on the beam neutral axis thus expression for t is obtained by considering the differential

$$t = \frac{\partial X}{\partial s} = \frac{\partial X}{\partial g}\frac{dg}{dh}\frac{dh}{ds} \tag{3-6}$$

g is the parameter in the shape function (Figure 6a). *h* and *s* denote length coordinate along the undeformed straight beam and the deformed bent beam respectively (Figure 6b, c). In addition *t* can also be acquired from the initial direction cosine vector *T* applied by rotation matrix *C* [22],

$$t = C \cdot T \tag{3-7}$$

where

$$C = \begin{bmatrix} \cos\theta & -\sin\theta \\ \sin\theta & \cos\theta \end{bmatrix} \quad T = \begin{bmatrix} \cos\theta_0 \\ \sin\theta_0 \end{bmatrix} \tag{3-8}$$

where θ_0 and θ are respectively the element's initial direction angle and the direction angle's change by the end of deformation.

$$t = C \cdot T = \begin{bmatrix} \cos(\theta + \theta_0) \\ \sin(\theta + \theta_0) \end{bmatrix} = \begin{pmatrix} \frac{\partial X_x}{\partial s} \\ \frac{\partial X_y}{\partial s} \end{pmatrix} \tag{3-9}$$

From (3-6) by chain rule one can find

$$\frac{\partial X}{\partial g} = \frac{ds}{dh}\frac{dh}{dg}t \tag{3-10}$$

For a special example initial straight beam element implies direction remains constant along the beam neutral axis such that $\theta_0(g) = \theta_{01} = \theta_{02}$, θ_{01} and θ_{02} are initial direction angles at beam ends. Using (3-10) one can get

$$\left.\frac{dX_{0x}}{dg}\right|_{g=-1} = \left.\frac{dX_{0x}}{dg}\right|_{g=1} = \frac{L}{2}\cos\theta_{01} = \frac{L}{2}\cos\theta_{02} = \frac{L}{2}\frac{X_{02x} - X_{01x}}{L} = \frac{X_{02x} - X_{01x}}{2} \tag{3-11}$$

$$\left.\frac{dX_{0y}}{dg}\right|_{g=-1} = \left.\frac{dX_{0y}}{dg}\right|_{g=1} = \frac{L}{2}\sin\theta_{01} = \frac{L}{2}\sin\theta_{02} = \frac{L}{2}\frac{X_{02y} - X_{01y}}{L} = \frac{X_{02y} - X_{01y}}{2} \tag{3-12}$$

where *L* is initial (before deformed) length of the straight beam defined as

$$L = \sqrt{(X_{02x} - X_{01x})^2 + (X_{02y} - X_{01y})^2} \tag{3-13}$$

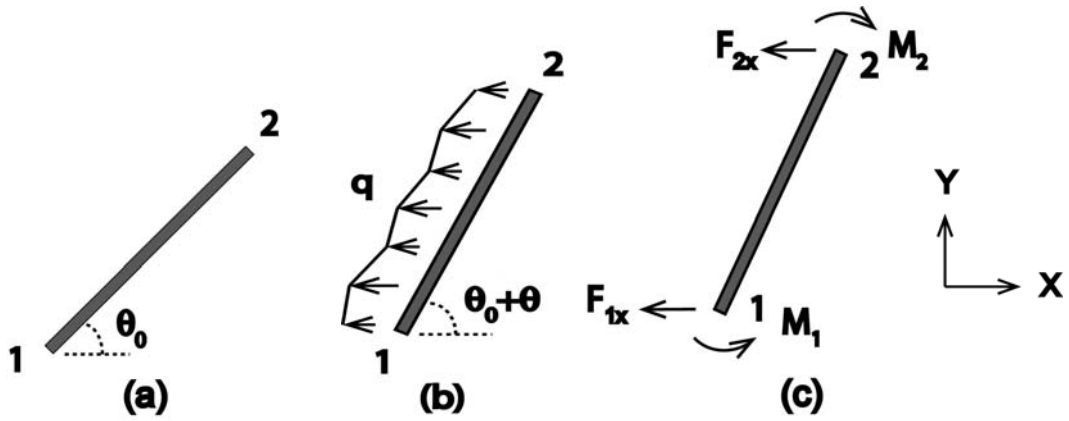

Figure 7 Viscous force applied on beam element. (a) Initial geometry and position of the beam (b) Deformed beam with external distributed load (c) Equivalent nodal force and moment on the deformed beam

According to (2-1) and using interpolation function (3-5), (3-6) and (3-10), k is negative and q is found to be

$$q = k\frac{\partial X_x}{\partial t}\sin(\theta_0+\theta)$$

$$= k\frac{\partial X_x}{\partial t}\frac{\partial X_y}{\partial s}$$

$$= k\left(N_1\frac{\partial X_{1x}}{\partial t} + N_2\frac{\partial X_{2x}}{\partial t} + N_3\frac{\partial\left(\frac{\partial X_{1x}}{\partial g}\right)}{\partial t} + N_4\frac{\partial\left(\frac{\partial X_{2x}}{\partial g}\right)}{\partial t}\right)\cdot$$

$$\left(\frac{\partial N_1}{\partial g}X_{1y} + \frac{\partial N_2}{\partial g}X_{2y} + \frac{\partial N_3}{\partial g}\left(\frac{\partial X_y}{\partial g}\right)\Big|_{g=-1} + \frac{\partial N_4}{\partial g}\left(\frac{\partial X_y}{\partial g}\right)\Big|_{g=1}\right)\frac{dg}{dh}\frac{dh}{ds}$$

$$= k\left(N_1\dot{X}_{1x} + N_2\dot{X}_{2x} + N_3\frac{ds}{dh}\frac{dh}{dg}\left(-\sin(\theta_1+\theta_0)\right)\dot{\theta}_1 + N_4\frac{ds}{dh}\frac{dh}{dg}\left(-\sin(\theta_2+\theta_0)\right)\dot{\theta}_2\right)\cdot$$

$$\left(\frac{\partial N_1}{\partial g}X_{1y}+\frac{\partial N_2}{\partial g}X_{2y}+\frac{\partial N_3}{\partial g}\frac{ds}{dh}\frac{dh}{dg}\sin(\theta_{01}+\theta_1)+\frac{\partial N_4}{\partial g}\frac{ds}{dh}\frac{dh}{dg}\sin(\theta_{02}+\theta_2)\right)\frac{dg}{dh}\frac{dh}{ds}$$

$$=k\left(N_1\dot{X}_{1x}+N_2\dot{X}_{2x}+N_3\frac{ds}{dh}\frac{L}{2}\left(-\sin\left(\theta_1+\theta_0\right)\right)\dot{\theta}_1+N_4\frac{ds}{dh}\frac{L}{2}\left(-\sin\left(\theta_2+\theta_0\right)\right)\dot{\theta}_2\right)\cdot$$

$$\left(\frac{\partial N_1}{\partial g}X_{1y}+\frac{\partial N_2}{\partial g}X_{2y}+\frac{\partial N_3}{\partial g}\frac{ds}{dh}\frac{L}{2}\sin\left(\theta_{01}+\theta_1\right)+\frac{\partial N_4}{\partial g}\frac{ds}{dh}\frac{L}{2}\sin\left(\theta_{02}+\theta_2\right)\right)\frac{2}{L}\frac{dh}{ds} \qquad (3\text{-}14)$$

where

$$\frac{\partial N_1}{\partial g}=\frac{1}{4}(3g^2-3) \qquad \frac{\partial N_2}{\partial g}=\frac{1}{4}(-3g^2+3)$$
$$\frac{\partial N_3}{\partial g}=\frac{1}{4}(3g^2-2g-1) \quad \frac{\partial N_4}{\partial g}=\frac{1}{4}(3g^2+2g-1) \qquad (3\text{-}15)$$

u and $\frac{\partial u}{\partial g}$, which are unknown variables resulted by deformation, are respectively nodal values.

Consider in energy formula (3-1) variations of y direction movements and rotations (δX_{1y}, δX_{2y}, $\delta\left(\frac{\partial X_{1y}}{\partial g}\right)$, $\delta\left(\frac{\partial X_{2y}}{\partial g}\right)$) are not contributing to the external work (3-1) because there is not external force in this direction so they are not included in the integral given as

$$W_E=\int_0^L qN_1\delta X_{1x}ds+\int_0^L qN_2\delta X_{2x}ds+\int_0^L qN_3\delta\left(\frac{\partial X_{1x}}{\partial g}\right)ds+\int_0^L qN_4\delta\left(\frac{\partial X_{2x}}{\partial g}\right)ds \qquad (3\text{-}16)$$

The virtual displacement in x is

$$N_1\delta X_{1x}+N_2\delta X_{2x}+N_3\delta\left(\frac{\partial X_{1x}}{\partial g}\right)+N_4\delta\left(\frac{\partial X_{2x}}{\partial g}\right) \qquad (3\text{-}17)$$

qds is the force applied on the area ds by viscous interaction.

Above is the virtual work done by surface viscous force. δX_{1x} and δX_{2x} are individually the arbitrary variations of displacements at node 1 and node 2. $\delta\left(\frac{\partial X_{1x}}{\partial g}\right)$ and $\delta\left(\frac{\partial X_{2x}}{\partial g}\right)$ are respectively the arbitrary variations of displacement derivatives at node 1 and node 2.

$$\int_0^L qN_1\delta X_{1x}ds = \int_{-1}^1 qN_1\delta X_{1x}\frac{ds}{dh}\frac{dh}{dg}dg$$
$$= \int_{-1}^1 qN_1\frac{ds}{dh}\frac{L}{2}dg\delta X_{1x} \tag{3-18}$$

$$\int_0^L qN_2\delta X_{2x}ds = \int_{-1}^1 qN_2\delta X_{2x}\frac{ds}{dh}\frac{dh}{dg}dg$$
$$= \int_{-1}^1 qN_2\frac{ds}{dh}\frac{L}{2}dg\delta X_{2x} \tag{3-19}$$

where final results of both the above equations can be acquired with chain rule.

$$\delta\left(\frac{\partial X}{\partial g}\right) = \frac{ds}{dh}\frac{dh}{dg}\delta t$$
$$= \frac{ds}{dh}\frac{dh}{dg}\begin{Bmatrix}\delta\cos(\theta+\theta_0)\\ \delta\sin(\theta+\theta_0)\end{Bmatrix} \tag{3-20}$$
$$= \frac{ds}{dh}\frac{dh}{dg}\begin{Bmatrix}-\sin(\theta+\theta_0)\\ \cos(\theta+\theta_0)\end{Bmatrix}\delta\theta$$

$$\int_0^L qN_3\delta\left(\frac{\partial X_{1x}}{\partial g}\right)ds = \int_{-1}^1 qN_3\left(-\sin\left(\theta_1+\theta_0\right)\right)\frac{ds}{dh}\frac{dh}{dg}\delta\theta_1\frac{ds}{dh}\frac{dh}{dg}dg$$
$$= \int_{-1}^1 qN_3\left(-\sin\left(\theta_1+\theta_0\right)\right)\frac{dh}{dg}\frac{dh}{dg}\frac{ds}{dh}\frac{ds}{dh}dg\delta\theta_1 \tag{3-21}$$
$$= \int_{-1}^1 qN_3\left(-\sin\left(\theta_1+\theta_0\right)\right)\frac{L^2}{4}\frac{ds}{dh}\frac{ds}{dh}dg\delta\theta_1$$

$$\int_0^L qN_4\delta\left(\frac{\partial X_{2x}}{\partial g}\right)ds = \int_{-1}^1 qN_4\left(-\sin\left(\theta_2+\theta_0\right)\right)\frac{ds}{dh}\frac{dh}{dg}\delta\theta_2\frac{ds}{dh}\frac{dh}{dg}dg$$
$$= \int_{-1}^1 qN_4\left(-\sin\left(\theta_2+\theta_0\right)\right)\frac{dh}{dg}\frac{dh}{dg}\frac{ds}{dh}\frac{ds}{dh}dg\delta\theta_2 \tag{3-22}$$
$$= \int_{-1}^1 qN_4\left(-\sin\left(\theta_2+\theta_0\right)\right)\frac{L^2}{4}\frac{ds}{dh}\frac{ds}{dh}dg\delta\theta_2$$

If beam is axially inextensible and incompressible, then $\frac{ds}{dh}=1$ is used in all equations. From (3-18)~(3-22) the global nodal force and nodal moment can be derived as follows:

$$F_{1x} = \int_{-1}^1 qN_1\frac{ds}{dh}\frac{L}{2}dg \tag{3-23}$$

$$F_{2x} = \int_{-1}^1 qN_2\frac{ds}{dh}\frac{L}{2}dg \tag{3-24}$$

$$M_1 = \int_{-1}^{1} qN_3\left(-\sin\left(\theta_1+\theta_0\right)\right)\frac{ds}{dh}\frac{ds}{dh}\frac{L^2}{4}dg \tag{3-25}$$

$$M_2 = \int_{-1}^{1} qN_4\left(-\sin\left(\theta_2+\theta_0\right)\right)\frac{ds}{dh}\frac{ds}{dh}\frac{L^2}{4}dg \tag{3-26}$$

q can be obtained from (3-14). In (3-23)~(3-26) N_1~N_4 are third order functions of g, and q is fifth order function of g, and totally the integral function is eighth order of g. One ought to use at least 5 Gauss interpolation points to get the accurate integral results.

$$\mathrm{F} = \begin{bmatrix} F_{1x} \\ F_{1y} \\ M_1 \\ F_{2x} \\ F_{2y} \\ M_2 \end{bmatrix} = \begin{bmatrix} F_{1x} \\ 0 \\ M_1 \\ F_{2x} \\ 0 \\ M_2 \end{bmatrix} \tag{3-27}$$

Vector F is the external load vector including horizontal nodal forces and nodal moments. The explicit expressions of F_{1x}, F_{2x}, M_1, M_2 can be directly obtained by integrals of (3-23)~(3-26).

3.2 Stiffness Matrix of Nodal Force

Viscous surface force q is a velocity dependent variable, and velocities are defined as the average value in the small time increment shown as

$$\frac{\partial u}{\partial t} = \frac{u_{current} - u_{previous}}{dtime} \qquad \frac{\partial \theta}{\partial t} = \frac{\theta_{current} - \theta_{previous}}{dtime} \tag{3-28}$$

Therefore sensitivities of displacement velocity and the rotation velocity about independent variables are expressed in terms of time increment as

$$\frac{\partial\left(\frac{\partial u}{\partial t}\right)}{\partial u} = \frac{1}{dtime} \qquad \frac{\partial\left(\frac{\partial \theta}{\partial t}\right)}{\partial \theta} = \frac{1}{dtime}$$
$$\frac{\partial\left(\frac{\partial u}{\partial t}\right)}{\partial \theta} = 0 \qquad \frac{\partial\left(\frac{\partial \theta}{\partial t}\right)}{\partial u} = 0 \tag{3-29}$$

Viscous surface force q's sensitivities about every independent variable are:

$$\frac{\partial q}{\partial u_{1x}} = \frac{kN_1}{dtime}\left(\frac{\partial N_1}{\partial g}X_{1y} + \frac{\partial N_2}{\partial g}X_{2y} + \frac{\partial N_3}{\partial g}\frac{ds}{dh}\frac{L}{2}\sin\left(\theta_{01}+\theta_1\right) + \frac{\partial N_4}{\partial g}\frac{ds}{dh}\frac{L}{2}\sin\left(\theta_{02}+\theta_2\right)\right)\frac{2}{L}\frac{dh}{ds} \tag{3-30}$$

$$\frac{\partial q}{\partial u_{1y}} = k\frac{\partial N_1}{\partial g}\left(N_1\dot{u}_{1x} + N_2\dot{u}_{2x} + N_3\frac{ds}{dh}\frac{L}{2}\left(-\sin\left(\theta_1+\theta_0\right)\right)\dot{\theta}_1 + N_4\frac{ds}{dh}\frac{L}{2}\left(-\sin\left(\theta_2+\theta_0\right)\right)\dot{\theta}_2\right)\frac{2}{L}\frac{dh}{ds} \tag{3-31}$$

$$\begin{aligned}\frac{\partial q}{\partial \theta_1} = k\Bigg(&N_3\frac{ds}{dh}\frac{L}{2}\left(-\cos\left(\theta_1+\theta_{01}\right)\right)\dot{\theta}_1 + \frac{N_3\frac{ds}{dh}\frac{L}{2}\left(-\sin\left(\theta_1+\theta_{01}\right)\right)}{dtime}\Bigg)\left(\frac{\partial N_1}{\partial g}\left(X_{01y}+u_{1y}\right)\right.\\ &\left.+\frac{\partial N_2}{\partial g}\left(X_{02y}+u_{2y}\right)+\frac{\partial N_3}{\partial g}\frac{ds}{dh}\frac{L}{2}\sin\left(\theta_{01}+\theta_1\right)+\frac{\partial N_4}{\partial g}\frac{ds}{dh}\frac{L}{2}\sin\left(\theta_{02}+\theta_2\right)\right)\frac{2}{L}\frac{dh}{ds}\\ &+k\left(N_1\dot{u}_{1x}+N_2\dot{u}_{2x}+N_3\frac{ds}{dh}\frac{L}{2}\left(-\sin\left(\theta_1+\theta_{01}\right)\right)\dot{\theta}_1+N_4\frac{ds}{dh}\frac{L}{2}\left(-\sin\left(\theta_2+\theta_{02}\right)\right)\dot{\theta}_2\right)\cdot\\ &\frac{\partial N_3}{\partial g}\frac{ds}{dh}\frac{L}{2}\cos\left(\theta_{01}+\theta_1\right)\frac{2}{L}\frac{dh}{ds}\end{aligned} \tag{3-32}$$

$$\frac{\partial q}{\partial u_{2x}} = \frac{kN_2}{dtime}\left(\frac{\partial N_1}{\partial g}X_{1y} + \frac{\partial N_2}{\partial g}X_{2y} + \frac{\partial N_3}{\partial g}\frac{ds}{dh}\frac{L}{2}\sin\left(\theta_{01}+\theta_1\right) + \frac{\partial N_4}{\partial g}\frac{ds}{dh}\frac{L}{2}\sin\left(\theta_{02}+\theta_2\right)\right)\frac{2}{L}\frac{dh}{ds} \tag{3-33}$$

$$\frac{\partial q}{\partial u_{2y}} = k\frac{\partial N_2}{\partial g}\left(N_1\dot{u}_{1x} + N_2\dot{u}_{2x} + N_3\frac{ds}{dh}\frac{L}{2}\left(-\sin\left(\theta_1+\theta_0\right)\right)\dot{\theta}_1 + N_4\frac{ds}{dh}\frac{L}{2}\left(-\sin\left(\theta_2+\theta_0\right)\right)\dot{\theta}_2\right)\frac{2}{L}\frac{dh}{ds} \tag{3-34}$$

$$\frac{\partial q}{\partial \theta_2} = k\left(N_4 \frac{ds}{dh}\frac{L}{2}\left(-\cos\left(\theta_2+\theta_{02}\right)\right)\dot{\theta}_2 + \frac{N_4 \frac{ds}{dh}\frac{L}{2}\left(-\sin\left(\theta_2+\theta_{02}\right)\right)}{dtime} \right)\left(\frac{\partial N_1}{\partial g} X_{1y} \right.$$
$$\left. + \frac{\partial N_2}{\partial g} X_{2y} + \frac{\partial N_3}{\partial g}\frac{ds}{dh}\frac{L}{2}\sin\left(\theta_{01}+\theta_1\right) + \frac{\partial N_4}{\partial g}\frac{ds}{dh}\frac{L}{2}\sin\left(\theta_{02}+\theta_2\right)\right)\frac{2}{L}\frac{dh}{ds}$$
$$+ k\left(N_1\dot{u}_{1x} + N_2\dot{u}_{2x} + N_3\frac{ds}{dh}\frac{L}{2}\left(-\sin\left(\theta_1+\theta_{01}\right)\right)\dot{\theta}_1 + N_4\frac{ds}{dh}\frac{L}{2}\left(-\sin\left(\theta_2+\theta_{02}\right)\right)\dot{\theta}_2 \right)\cdot$$
$$\frac{\partial N_4}{\partial g}\frac{ds}{dh}\frac{L}{2}\cos\left(\theta_{02}+\theta_2\right)\frac{2}{L}\frac{dh}{ds}$$

(3-35)

The load stiffness about the each freedom degree is expressed as follows,

$$\mathrm{K} = \begin{bmatrix} K_{11} & K_{12} & K_{13} & K_{14} & K_{15} & K_{16} \\ K_{21} & K_{22} & K_{23} & K_{24} & K_{25} & K_{26} \\ K_{31} & K_{32} & K_{33} & K_{34} & K_{35} & K_{36} \\ K_{41} & K_{42} & K_{43} & K_{44} & K_{45} & K_{46} \\ K_{51} & K_{52} & K_{53} & K_{54} & K_{55} & K_{56} \\ K_{61} & K_{62} & K_{63} & K_{64} & K_{65} & K_{66} \end{bmatrix} \tag{3-36}$$

Where the component K_{ij} of the stiffness matrix ***K*** is the force required at No. i freedom degree in order that a unit displacement is applied at No. j freedom degree. Therefore, K_{ij} can be expressed in the form of derivative,

$$K_{ij} = \frac{\partial F_i}{\partial u_j} \tag{3-37}$$

Note that because F_{1y} and F_{2y} are permanently zeros then:

$$K_{21} = K_{22} = K_{23} = K_{24} = K_{25} = K_{26} = 0 \tag{3-38}$$
$$K_{51} = K_{52} = K_{53} = K_{54} = K_{55} = K_{56} = 0 \tag{3-39}$$

The complete expressions of every component in matrix ***K*** are derived from (3-23) ~ (3-26) as follows:

$$K_{11}=\int_{-1}^{1}\frac{\partial q}{\partial u_{1x}}N_1\frac{ds}{dh}\frac{L}{2}dg \qquad K_{12}=\int_{-1}^{1}\frac{\partial q}{\partial u_{1y}}N_1\frac{ds}{dh}\frac{L}{2}dg \qquad K_{13}=\int_{-1}^{1}\frac{\partial q}{\partial \theta_1}N_1\frac{ds}{dh}\frac{L}{2}dg$$

$$K_{14}=\int_{-1}^{1}\frac{\partial q}{\partial u_{2x}}N_1\frac{ds}{dh}\frac{L}{2}dg \qquad K_{15}=\int_{-1}^{1}\frac{\partial q}{\partial u_{2y}}N_1\frac{ds}{dh}\frac{L}{2}dg \qquad K_{16}=\int_{-1}^{1}\frac{\partial q}{\partial \theta_2}N_1\frac{ds}{dh}\frac{L}{2}dg$$

$$K_{41}=\int_{-1}^{1}\frac{\partial q}{\partial u_{1x}}N_2\frac{ds}{dh}\frac{L}{2}dg \qquad K_{42}=\int_{-1}^{1}\frac{\partial q}{\partial u_{1y}}N_2\frac{ds}{dh}\frac{L}{2}dg \qquad K_{43}=\int_{-1}^{1}\frac{\partial q}{\partial \theta_1}N_2\frac{ds}{dh}\frac{L}{2}dg$$

$$K_{44}=\int_{-1}^{1}\frac{\partial q}{\partial u_{2x}}N_2\frac{ds}{dh}\frac{L}{2}dg \qquad K_{45}=\int_{-1}^{1}\frac{\partial q}{\partial u_{2y}}N_2\frac{ds}{dh}\frac{L}{2}dg \qquad K_{46}=\int_{-1}^{1}\frac{\partial q}{\partial \theta_2}N_2\frac{ds}{dh}\frac{L}{2}dg$$

$$K_{31}=\int_{-1}^{1}\frac{\partial q}{\partial u_{1x}}N_3\left(-\sin\left(\theta_1+\theta_0\right)\right)\frac{ds}{dh}\frac{ds}{dh}\frac{dh}{dg}\frac{dh}{dg}dg$$

$$K_{32}=\int_{-1}^{1}\frac{\partial q}{\partial u_{1y}}N_3\left(-\sin\left(\theta_1+\theta_0\right)\right)\frac{ds}{dh}\frac{ds}{dh}\frac{dh}{dg}\frac{dh}{dg}dg$$

$$K_{33}=\int_{-1}^{1}\left[\frac{\partial q}{\partial \theta_1}N_3\left(-\sin\left(\theta_1+\theta_0\right)\right)+qN_3\left(-\cos\left(\theta_1+\theta_0\right)\right)\right]\frac{ds}{dh}\frac{ds}{dh}\frac{dh}{dg}\frac{dh}{dg}dg$$

$$K_{34}=\int_{-1}^{1}\frac{\partial q}{\partial u_{2x}}N_3\left(-\sin\left(\theta_1+\theta_0\right)\right)\frac{ds}{dh}\frac{ds}{dh}\frac{dh}{dg}\frac{dh}{dg}dg$$

$$K_{35}=\int_{-1}^{1}\frac{\partial q}{\partial u_{2y}}N_3\left(-\sin\left(\theta_1+\theta_0\right)\right)\frac{ds}{dh}\frac{ds}{dh}\frac{dh}{dg}\frac{dh}{dg}dg$$

$$K_{36}=\int_{-1}^{1}\frac{\partial q}{\partial \theta_2}N_3\left(-\sin\left(\theta_1+\theta_0\right)\right)\frac{ds}{dh}\frac{ds}{dh}\frac{dh}{dg}\frac{dh}{dg}dg$$

$$K_{61}=\int_{-1}^{1}\frac{\partial q}{\partial u_{1x}}N_4\left(-\sin\left(\theta_2+\theta_0\right)\right)\frac{ds}{dh}\frac{ds}{dh}\frac{dh}{dg}\frac{dh}{dg}dg$$

$$K_{62}=\int_{-1}^{1}\frac{\partial q}{\partial u_{1y}}N_4\left(-\sin\left(\theta_2+\theta_0\right)\right)\frac{ds}{dh}\frac{ds}{dh}\frac{dh}{dg}\frac{dh}{dg}dg$$

$$K_{63}=\int_{-1}^{1}\left[\frac{\partial q}{\partial \theta_1}N_4\left(-\sin\left(\theta_2+\theta_0\right)\right)\right]\frac{ds}{dh}\frac{ds}{dh}\frac{dh}{dg}\frac{dh}{dg}dg$$

$$K_{64} = \int_{-1}^{1} \frac{\partial q}{\partial u_{2x}} N_4 \left(-\sin\left(\theta_2 + \theta_0\right)\right) \frac{ds}{dh}\frac{ds}{dh}\frac{dh}{dg}\frac{dh}{dg} dg$$

$$K_{65} = \int_{-1}^{1} \frac{\partial q}{\partial u_{2y}} N_4 \left(-\sin\left(\theta_2 + \theta_0\right)\right) \frac{ds}{dh}\frac{ds}{dh}\frac{dh}{dg}\frac{dh}{dg} dg$$

$$K_{66} = \int_{-1}^{1} \left[\frac{\partial q}{\partial \theta_2} N_4 \left(-\sin\left(\theta_2 + \theta_0\right)\right) + qN_4 \left(-\cos\left(\theta_2 + \theta_0\right)\right) \right] \frac{ds}{dh}\frac{ds}{dh}\frac{dh}{dg}\frac{dh}{dg} dg \tag{3-40}$$

$$\mathrm{K} = \begin{bmatrix} K_{11} & K_{12} & K_{13} & K_{14} & K_{15} & K_{16} \\ 0 & 0 & 0 & 0 & 0 & 0 \\ K_{31} & K_{32} & K_{33} & K_{34} & K_{35} & K_{36} \\ K_{41} & K_{42} & K_{43} & K_{44} & K_{45} & K_{46} \\ 0 & 0 & 0 & 0 & 0 & 0 \\ K_{61} & K_{62} & K_{63} & K_{64} & K_{65} & K_{66} \end{bmatrix} \tag{3-41}$$

The above equations are the nodal forces and moments and their stiffness. They are used to solve the system of equations by Newton-Raphson method. The load behaviors of the loading element are thus fully determined by the stiffness matrix *K* and the right-hand side nodal force vector *F* in the finite element formulations. Implementation of these formulations in the finite element schemes to solve the problem of beam buckle propagation in a viscous medium will be discussed in Chapter 4.

Chapter 4 Evolution of Progressive Buckles

The goal is to numerically simulate the beam deformation under axial compression with the lateral viscous force. It is found that the beam presents the regular progressive buckles from bottom end to the top end; that is, each similar sized buckle is forming at a constant rate in sequence and the indenting force is found at a constant level during the sequenced buckle forming process. Dimensional analysis is used to derive the formulas for plateau load, buckle forming rate, buckle wave length from beam bending stiffness, viscosity and indenting rate. The three formulas' three independent coefficients are determined from the FEM simulations. The geometric and material parameters used in simulations but not included in the dimensional analysis are tested and proved to have notable influences on the beam deformation results.

4.1 Dimension Analysis

Undoubtedly the nanotube mechanical response is relying on the indenting rate, nanotube bending stiffness and nanoturf's viscosity. Different compression buckle behaviors can be achieved by the combinations of the above three parameters. The purpose is to quantify the compression rate, tube bending stiffness and viscous property influences on the buckle length, self contact rate and buckle plateau force so as to give an explicit quantitative formula for the specific nanotube turf.

However, for the complex buckle behavior with distributed viscous force the beam response formula would be less easily derived in terms of the continuum mechanics concepts. Beam surface viscous force is the function of instant beam's orientation and beam position change in the time increment, and reversely the viscous force will affect the beam geometry or

curvature result. This is a highly complex process which requires nonlinear iterations to get each increment solution. A procedure based on *dimensional analysis* is introduced to derive the essential relations of interest from the input parameters. Dimensional analysis is a tool to find the relation between the output variables and properties of physical quantities. When the explicit formulas from arbitrary input records to output phenomenon variables are not obvious, dimensional analysis techniques provide an efficient approach to acquire estimates which require the formula's unit to match on both sides. Next the dimensional analysis procedure is formulated to derive the expressions from inputs to outputs, and FEM simulations will be used to determine the unknown constants.

Table 1 Units of the input and output parameters in terms of standard units *F*, *T*, *L*. Force unit: *F*, time unit: *T*, length unit *L*.

Variable	EI	K	R	P	λ	τ
Unit	$F \cdot L^2$	$\frac{F \cdot T}{L^2}$	$\frac{L}{T}$	F	L	T

Table 1 lists the units of three input variables *EI*, *K*, *R* and three output variables *P*, λ, τ. in terms of standard units denoted by force *F*, time *T*, length *L*. Consider a group of 4 variables *EI*, *K*, *R* and *P*. Among them 3 out of 4 variables are independent and can be arbitrarily set with the remaining one variable being determined by others. Since *EI*, *K*, *R* are material properties and loading condition which can be easily controlled, one can readily derive *P* shown by (4-1) as long as to make *P** unitless. Following the same procedure other two output variables λ and τ can be obtained as (4-2) and (4-3) individually.

$$P^* = \frac{P}{K^{\frac{2}{3}} R^{\frac{2}{3}} (EI)^{\frac{1}{3}}} \tag{4-1}$$

$$\lambda^* = \frac{\lambda}{\left(\frac{EI}{KR}\right)^{\frac{1}{3}}} \tag{4-2}$$

$$\tau^* = \frac{\tau}{\frac{(EI)^{\frac{1}{3}}}{K^{\frac{1}{3}} R^{\frac{4}{3}}}} \tag{4-3}$$

In this work, unknown deformation constants are defined as the constants P^*, λ^*, τ^*. The buckle deformations obtained from the axial compression tests are used to quantify plateau load, buckle length and self contact interval rate under various compression rates, nanoturf viscosities and beam bending stiffness. The compression rate should not be too slow or too fast compared with bending stiffness and viscosity. Extremely slow rate will make the buckle wave length exceed the total beam length thus only the first mode buckle would appear and there would not have differences for the different rates. Extremely fast rate would make the buckle wave length too short. Due to the limited amount of elements too small buckles would not be observed and cause numerical difficulties.

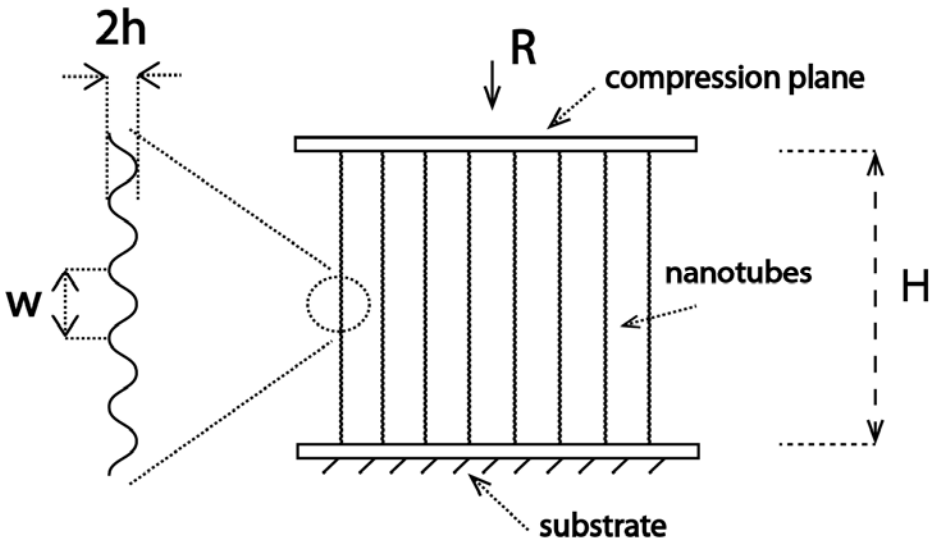

Figure 8 Schematic of the geometry model

4.2 Nanotube Compression Analysis

The system consists of vertically placed nanotubes free standing on the rigid substrate while under uniform compression at top surface by rigid indenting plane. Each vertically placed nanotube is modeled as two-dimensional isotropic linear elastic Euler beam element. The constant beam properties are characterized as area stiffness *EA*, bending stiffness *EI*. Viscosity generated by proximate nanotubes impacting interaction is denoted as *K*. According to the observation that each nanotube in the bundles presents the natural periodic waviness rather than pure straight [19], thus beam geometry is assumed presenting the shape at periodic sinusoidal function of wave length *w* and wave magnitude *h*. To avoid the geometry eccentricity effect, the whole beam of total height *H* comprises complete sinusoidal periods and the beam symmetric axis is aligned vertically and orthogonal to both the substrate and compression plane. Compression test is done as compression plane moving downward distance of *D* and duration of

d at a constant displacement increment rate *R=D/d*, and at any instant time compression plane remains fixed in horizontal and without any rotation. The substrate is fixed in all degrees of freedom. Cao et al. [7] found bottom end is different from top end in terms of density and stiffness. As to agree with this observation, the bottom end is set free rotation and free displacement in the two dimensional plane while the top end cannot move along the horizontal direction. The top end being more constrained than the bottom can be explained as the top end is of higher density than the bottom end. The nanotube can not penetrate the substrate and the compression plane whereas contacts between the nanotube and substrate and self contacts of each nanotube are frictionless. These configurations are shown in Figure 8.

In the following example beam material parameter is axial stiffness $\overline{H}=\frac{H}{(EI)^{1/3}(K\cdot R)^{-1/3}}$ $=100$, $\overline{h}=\frac{h}{(EI)^{1/3}(K\cdot R)^{-1/3}}=0.01$, $\overline{w}=\frac{w}{(EI)^{1/3}(K\cdot R)^{-1/3}}=1$, $\overline{EA}=\frac{EA}{(K\cdot R)^{2/3}(EI)^{1/3}}=6666.666667$. It should be mentioned that none of values are real physical parameters and dimensions of the nanotube, and they are selected such that firstly the natural sine shape function wave magnitude and length should be chosen smaller enough compared with the buckles resulted from the viscosity *K*, bending stiffness *EI* and compression rate *R* in order to avoid any artificial shape that would regulate the bulked shape after deformation, and secondly the buckles should be enough smaller than the beam total length in order to generate sufficient quantity of buckles to compare their properties. It is noted that these constants are selected somewhat arbitrarily which do not represent the real experimental conditions whereas this example's purpose is only to numerically test and validate the proposed deformation mechanism's accuracy.

Figure 9 shows localized buckle starts to develop around the bottom end, stabilizes as the fixed folding size, evolves to the adjacent part along the length, and successive buckle overlaps

on the previous fold repeating the same process time after time. Deformation front indicative of boundary by distinguishing portion deformed from that undeformed occurs in a region immediately ahead of the buckles. This process continues to develop until the whole length becomes folded. Indication that natural waves are small enough relative to the buckle size implies their negligible influence on the buckle shape.

The evolving localized deformation is the result of effects from the transverse load, beam bending stiffness and boundary conditions. Analysis suggests that elastic beam subjected to axial compression and lateral viscous confinement deforms by the balance of internal bending moment and transverse confinement. Upon high bending stiffness and low transverse confinement, large buckle or small curvature will form because low confinement is not able to stabilize smaller buckles. Upon low bending stiffness and high transverse confinement small buckle or large curvature would form because limited bending stiffness is not capable to generate the required moment to resist that induced by confinement. Only moderate level buckle size can be formed to balance the lateral confinement force. This is the case that beam deflection influences the transverse force which inversely limits the deflection magnitude, thus only suitable deflection can balance the internal force with the external confinement. The progressive buckle growth is related with the nonuniform boundaries at both ends. Compression of a beam results in the deflection of bottom free end thus forming a bending shape at a moderate size there. This bending shape will form an arc of instable state. At the transition location where beam path changes from the bending to straight is the most weakening point and the deformation prefers occur there than other locations. The vertical force will further bend this arc until it is fully collapsed. And then next period follows up the previous one at the same behavior. Buckles will collapse one by one in sequence.

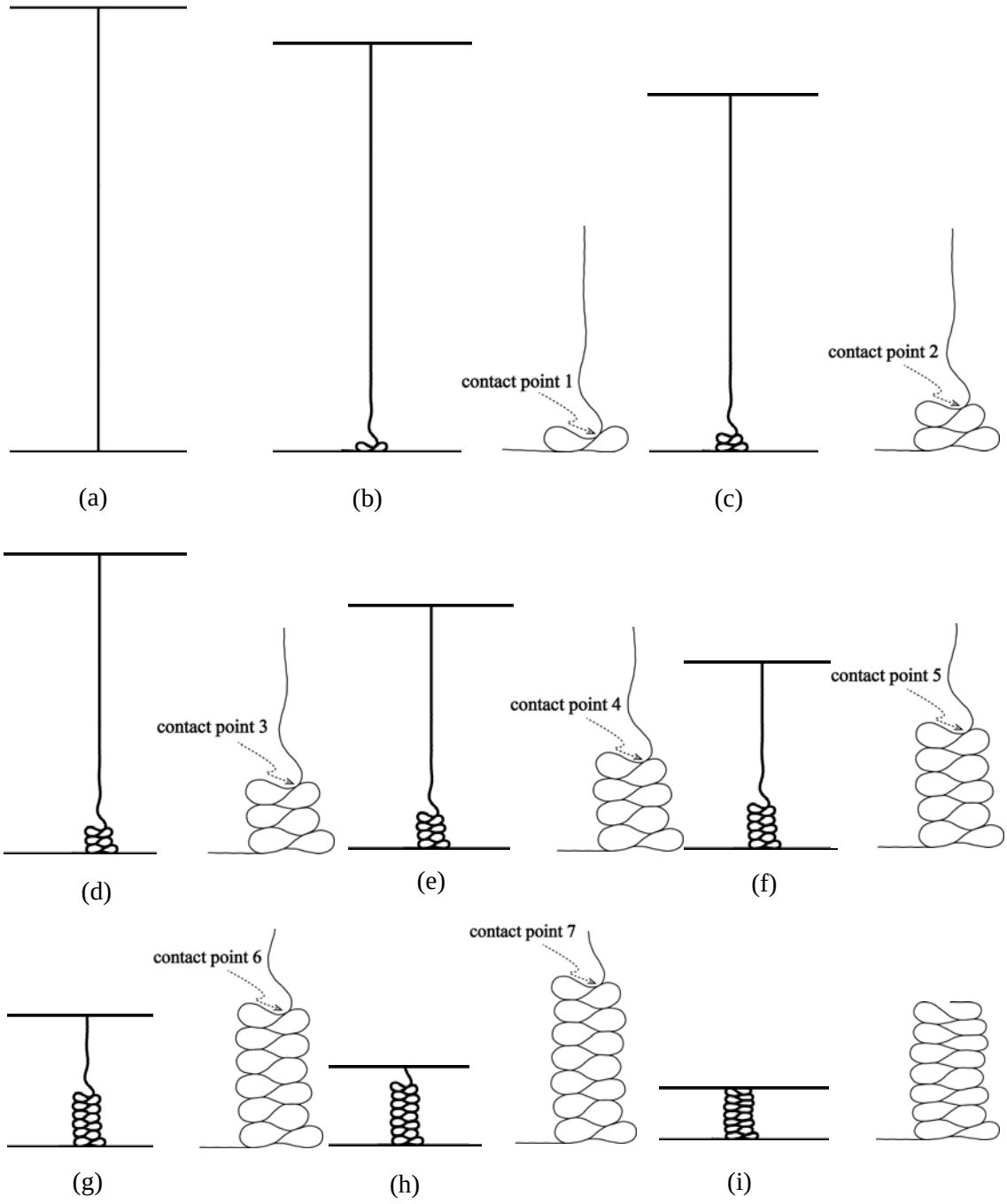

Figure 9 Deformation shape of beam at each completion of the buckle folding.

The Vdw force is strong enough to fix self folding [23]. The attractive vdw force exists between the tubes and it is a short range force as long as the distance small enough it can obtain

the maximum value to make the contacted tubes difficult to separate. During the compression the bounce back force is very small relative to the vdw attraction thus they can not separate away and always bonded by vdw force. It is noted vertical contact is different from the horizontal contact. vdw force is much smaller than the force needed to lock the contact between neighboring different tubes. It is assumed the vdw force is not large enough to limit the lateral relative movement outside folding region. On the other hand, from Figure 9 one can find contact surfaces are mostly along the horizontal direction, therefore the contact force is vertical force. The tube space density of folded regions becomes significantly large as can be treated that the occupancy of tubes is saturated for the space, thus no additional tube is allowed to push into the folded region. After self contact occurrence, the contacted parts can neither go away and separate from the folded tube for vdw adhesion nor go into the folded region thus in modeling non-separation condition after contact is enforced.

Every locked fold is favored in the lying horizontal position rather than on a vertical standing position can be explained as the lying position possesses the smallest vertical area projection by which the projection on the vertical plane is a minimum, and the viscous work is the lowest because the viscous force is a minimum for a unit horizontal translation. The closed fold is stably trapped on the lying position instead of standing position. Because the viscosity is constant then the deviation resulted to one side is equal to the deviation resulted to the other side. Therefore the whole symmetrical line remains unchanged in rotation and translation. Thus one can find the buckle folds pile up layer by layer vertically without deviation.

Regular buckles are found to form layer by layer. Since the contact can not separate after occurrence of contact, as long as one fold is formed and fixed it becomes the solid support and almost does not deform albeit at most there is a very small deformation of shape change. Next

buckle bends on the basis of the previous one. Then its pure effect is similar to lift the substrate one buckle layer up. Next step deformation should be same to the previous one, thus time used for each contact interval is same to the previous one. In Table 2 each buckle length and self contact rate are listed as nearly constant values. Each buckle length is defined as distance from one contact point going along the beam axis to the next upward contact point (Figure 9), and self contact interval rate is the time difference from one contact point to the next. At the buckle forming period the compression load is acting to bend each fold and each fold is same therefore the compression force should be nearly constant across the buckle period as shown in Figure 10.

In fact after the buckle deformation there are more tubes concentrated in the bottom region, so the viscosity is increased there. But since the condition of no separation after contact is applied then the closed loop of tube can not have further influence on the undeformed beam part. The only function of the finished buckle folds is supporting the upper part as a rigid body (Even the closed buckle part can obtain slight deformation but that deformation space is very limited.) lying on the substrate. Therefore using the constant viscosity *K* across the height for the whole process is not so severe.

Table 2 Buckle forming rate and buckle length directly measured from beam deformation shape. Buckle forming rate is defined as the duration between adjacent contact points. Buckle length is defined as the distance along the beam between adjacent contact points. Contact points are defined in Figure 9.

Contact Interval	1~2	2~3	3~4	4~5	5~6	6~7
$\bar{\tau} = \frac{\tau K^{\frac{1}{3}} R^{\frac{4}{3}}}{(EI)^{\frac{1}{3}}}$	10.089	11.160	10.890	11.010	10.980	9.990
$\bar{\lambda} = \frac{\lambda (KR)^{\frac{1}{3}}}{(EI)^{\frac{1}{3}}}$	11.900	12.900	12.400	12.700	12.700	12.100

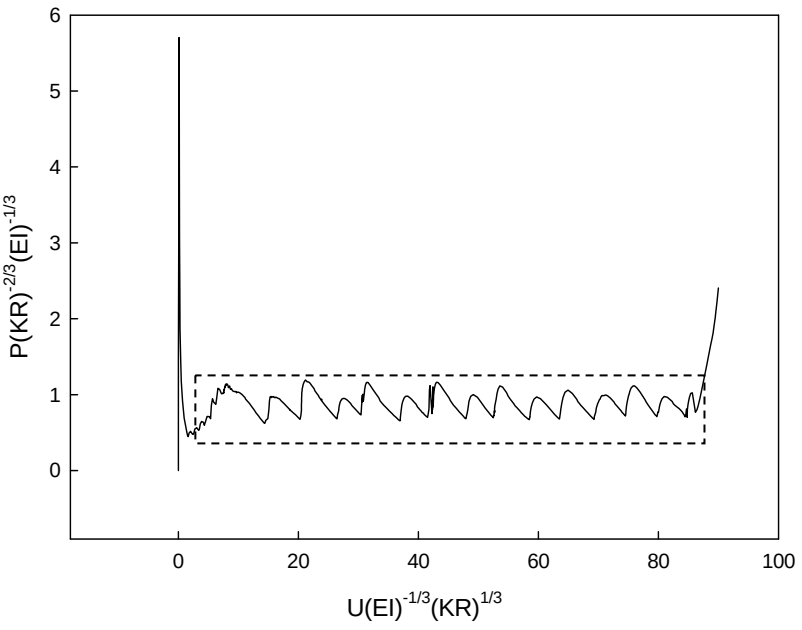

Figure 10 Indenting force vs. indenting displacement. Force in the dash line box is oscillating around a constant average value which is defined as plateau load.

In order to determine P^*, τ^*, λ^* in (4-1) ~ (4-3) multiple simulations are done with the same geometry and boundary conditions. Boundary conditions, contact conditions, loading methods are consistent with the previous example. In agreement with Figure 8, the beam geometry, beam material properties, friction resistance, loading conditions are characterized by total height, natural wave length and wave magnitude, bending stiffness, area stiffness, viscosity and compression rate. In the simulations H, h, w, EA are kept constant and EI, K, R are varying at constant interval. In the first group to change EI, $\overline{H} = \frac{H}{(EI)^{1/3}(K \cdot R)^{-1/3}} \in [100, 144.224957]$, $\overline{h} =$

$\frac{\mathrm{h}}{(\mathrm{EI})^{1/3}(\mathrm{K}\cdot\mathrm{R})^{-1/3}} \in [0.01,\ 0.0144225]$, $\bar{w} = \frac{\mathrm{w}}{(\mathrm{EI})^{1/3}(\mathrm{K}\cdot\mathrm{R})^{-1/3}} \in [1,\ 1.442250]$, $\overline{EA} = \frac{\mathrm{EA}}{(\mathrm{K}\cdot\mathrm{R})^{2/3}(\mathrm{EI})^{1/3}}$ $\in [6666.666667, 9614.997135]$; In the second group to change viscosity K, $\bar{H} = \frac{\mathrm{H}}{(\mathrm{EI})^{1/3}(\mathrm{K}\cdot\mathrm{R})^{-1/3}}$ $\in [100,\ 144.224957]$, $\bar{h} = \frac{\mathrm{h}}{(\mathrm{EI})^{1/3}(\mathrm{K}\cdot\mathrm{R})^{-1/3}} \in [0.01,\ 0.0144225]$, $\bar{w} = \frac{\mathrm{w}}{(\mathrm{EI})^{1/3}(\mathrm{K}\cdot\mathrm{R})^{-1/3}} \in [1,$ $1.442250]$, $\overline{EA} = \frac{\mathrm{EA}}{(\mathrm{K}\cdot\mathrm{R})^{2/3}(\mathrm{EI})^{1/3}} \in [3204.999045,\ 6666.666667]$; In the third group to change velocity R, $\bar{H} = \frac{\mathrm{H}}{(\mathrm{EI})^{1/3}(\mathrm{K}\cdot\mathrm{R})^{-1/3}} \in [100,\ 144.224957]$, $\bar{h} = \frac{\mathrm{h}}{(\mathrm{EI})^{1/3}(\mathrm{K}\cdot\mathrm{R})^{-1/3}} \in [0.01,\ 0.0144225]$, $\bar{w} = \frac{\mathrm{w}}{(\mathrm{EI})^{1/3}(\mathrm{K}\cdot\mathrm{R})^{-1/3}} \in [1, 1.442250]$, $\overline{EA} = \frac{\mathrm{EA}}{(\mathrm{K}\cdot\mathrm{R})^{2/3}(\mathrm{EI})^{1/3}} \in [3204.999045, 6666.666667]$.

Refer to Figure 10, in the dash line box the compression force is oscillating around the constant. Buckle plateau load is defined as $F = \frac{\int_{x_1}^{x_2} f(x)dx}{x_2 - x_1}$, where x_1 and x_2 are lower and upper bounding displacements of the dash box. With the increasing difference $x_2 - x_1$ and $f(x)$ as a periodic function of x, F would converge to the constant value. As long as the difference of x_2 and x_1 is large enough, F would be accurate enough. After the initial peak force at buckling, many subsequent peak forces exist, each of which is associated with a fold on the deformed beam. Buckle wave length is defined as the along axial distance between adjacent contact points in Figure 9, and averaged wave length obtained from 5 continuous folds starting from contact point 1 is used in the formula. In similar way the contact interval rate (buckle forming rate) is defined as the adjacent contact interval in Figure 9 and averaged value of 5 continuous contacts starting from contact point 1 is used in the formula. The constants of P^*, λ^*, τ^* are obtained from the linear regression least square analysis of Figure 11, Figure 12, Figure 13 as

$$P = 0.8874 K^{\frac{2}{3}} R^{\frac{2}{3}} (EI)^{\frac{1}{3}} \tag{4-4}$$

$$\lambda = 12.3641 \left(\frac{EI}{KR} \right)^{\frac{1}{3}} \tag{4-5}$$

$$\tau = 10.6349 \frac{(EI)^{\frac{1}{3}}}{K^{\frac{1}{3}} R^{\frac{4}{3}}} \tag{4-6}$$

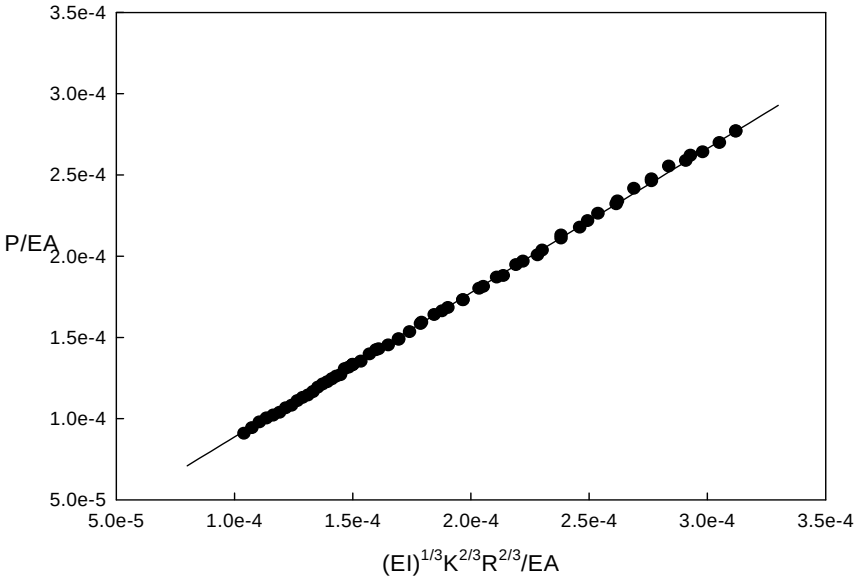

Figure 11 Normalized plateau load formula. P, EI, K and R are plateau load, beam bending stiffness, nanoturf viscosity and indenting rate respectively. Solid dots are FEM results, and solid line is fitted from FEM results.

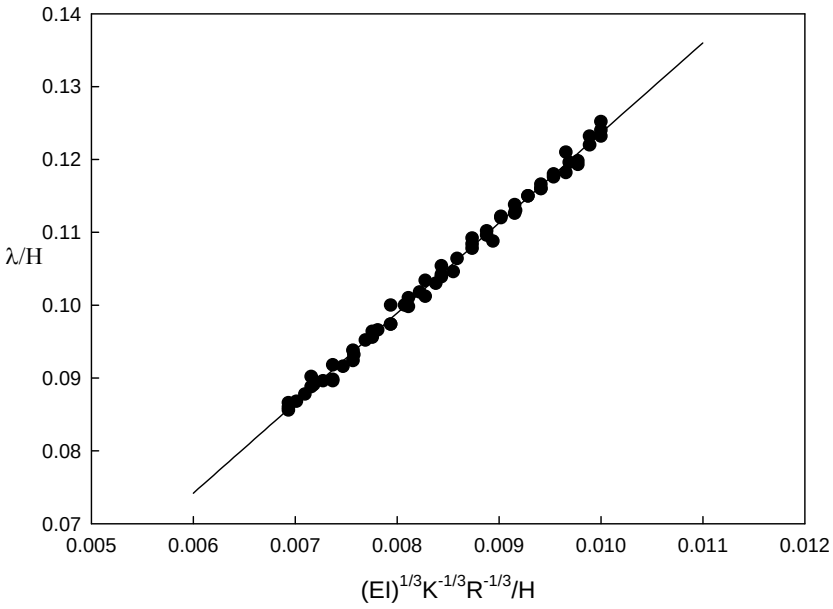

Figure 12 Normalized buckle wave length formula. λ, EI, K and R are buckle length, beam bending stiffness, nanoturf viscosity and indenting rate respectively. Solid dots are FEM results, and solid line is fitted from FEM results.

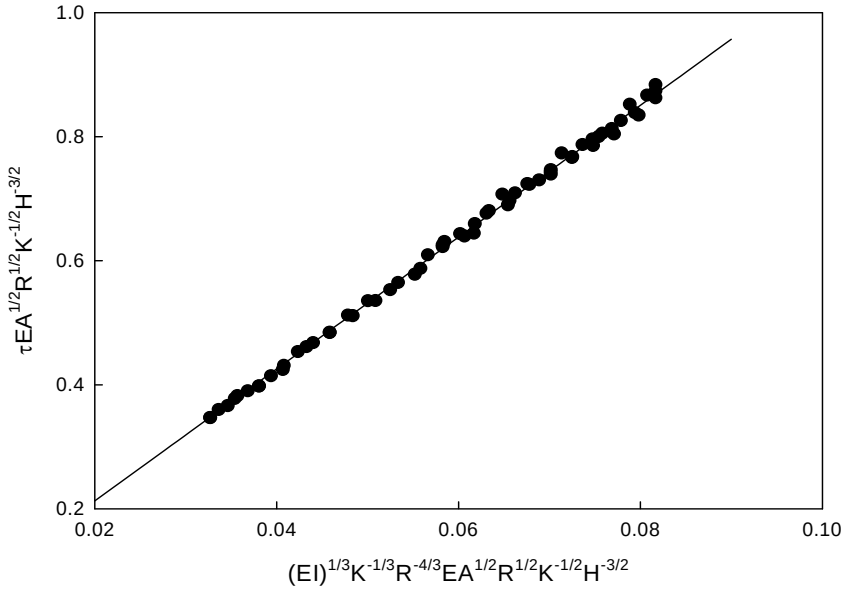

Figure 13 Normalized buckle forming rate. τ, EI, K and R are buckle forming rate, beam bending stiffness, nanoturf viscosity and indenting rate respectively. Solid dots are FEM results, and solid line is fitted from FEM results.

To elucidate bending stiffness *EI* influence on beam buckling behavior we focus on the change of *EI* with *K* and *R* remaining constant. The interplay of bending stiffness *EI*, viscosity *K* and compression rate *R* leads to the formation of buckles at a moderate size. Upon increasing of bending stiffness *EI* with viscosity *K* and compression *R* remaining unchanged, current lateral force and compression force can not stabilize current buckle shape for the unbalanced internal bending moment resulted from increased bending stiffness. In order to relax the over increased internal bending moment, bending curvature decreases a little leading to formation of a larger buckle (Figure 12) arc length but the effective internal moment is still increased at limited value to balance the external moment induced by compression and lateral force. As to make energy, including elastic and viscous energy, increase at the minimum amount homogenized simultaneous increase will occur for both the compression (Figure 11) and lateral force until the new equilibrium is reached. The total beam length remains unchanged but increasing size of each buckle leads to reduction of number of buckles. As compression rate and compression duration remain unchanged and each self contact rate is same as defined in section 4.2, then self contact rate will be increased (Figure 13).

To elucidate viscosity *K* influence on beam buckling behavior we focus on the change of *K* with *EI* and *R* remaining constant. The interplay of bending stiffness *EI*, viscosity *K* and compression rate *R* leads to the formation of buckles at a moderate size. Upon increasing of viscosity *K* with bending stiffness *EI* and compression *R* remaining unchanged, bending stiffness induced internal moment can not balance the external moment caused by lateral and compression force for the current bending shape attributed to the increased viscosity. In order to stiffen the current soft structure and slow down the increasing lateral force, the lateral deflection decreases and bending curvature increases a little leading to formation of a smaller buckle arc length

(Figure 12) resulting the increasing of internal moment at limited value to balance the external moment induced by compression and lateral force. As to make energy, including elastic and viscous energy, increase at the minimum amount homogenized simultaneous increase will occur for both compression (Figure 11) and lateral force until the new equilibrium is reached. The total beam length remains unchanged but decreasing size of each buckle leads to increase of number of buckles. As compression rate and compression duration remain unchanged and each self contact rate is defined as same in section 4.2, then self contact rate will be decreased (Figure 13).

To elucidate compression velocity *R* influence on beam buckling behavior we focus on the change of *R* with *EI* and *K* remaining constant. The interplay of bending stiffness *EI*, viscosity *K* and compression rate *R* leads to the formation of buckles at a moderate size. Upon increasing of compression rate *R* with bending stiffness *EI* and viscosity *K* remaining unchanged, bending stiffness induced internal moment can not balance additional external moment caused by increased lateral force due to fast lateral expansion. The increased lateral force acts as the inhibition of current buckles. In order to stiffen the current soft structure and slow down the increasing lateral force, the bending curvature increases a little leading to formation of a smaller buckle arc length (Figure 12) resulting the increasing of internal moment at limited value to balance the external moment induced by compression and lateral force. As to make energy, including elastic and viscous energy, increase at the minimum amount homogenized simultaneous increase will occur for both the compression (Figure 11) and lateral force until the new equilibrium is reached. The total beam length remains unchanged but decreasing size of each buckle leads to increase of number of buckles. As compression rate increased (i.e. compression duration decreased) and each self contact rate is defined same as in section 4.2, then self contact rate will be decreased (Figure 13).

It is noted that the random selected values total height, area stiffness, perturbed wave length and wave magnitude are required in the simulations. Their influences on the results are to be investigated.

4.3 Influences of Nanotube Parameters on Buckle Deformations

In order to match beam model with real nanotube geometry in nanoturf, the beam is regulated to be in the sinusoidal shape defined by parameters of natural wave length *w* and wave magnitude *h*. Additionally, in order to use the Euler beam element the beam axial stiffness *EA* is a necessary input parameter to run the model. Thirdly, the nanotube's total height *H* is chosen arbitrarily as the model information. Although these 4 parameters do not appear in the relations (4-4) ~ (4-6), it is necessary to investigate if the influences of them fall within the negligible scope for the outputs. All three outputs of buckle plateau force, buckle forming rate and buckle folding length directly measured from each variation of nanotube parameters are compared by those values obtained theoretically with same contact conditions, material properties, geometry configurations, and boundary conditions as defined in section 4.2. According to (4-4) ~ (4-6) buckle plateau force *P*, buckle forming rate τ and buckle folding length λ can be acquired.

At moderate range each of these four parameters has negligible influence on nanotube deformation process, but beyond that they can result in irregular deformations that do not follow progressive buckles ascribed to physical or numerical issues.

Total length *H* effect is investigated in the following. In Figure 14 parameters are set as $\overline{H} = \frac{H}{(EI)^{1/3}(K\cdot R)^{-1/3}}$ =172.354775, 193.899122, 215.443469, 236.987816, 258.532163, 280.076510, 301.620857; $\overline{h} = \frac{h}{(EI)^{1/3}(K\cdot R)^{-1/3}}$ =0.021544; $\overline{w} = \frac{w}{(EI)^{1/3}(K\cdot R)^{-1/3}}$ =2.154435; $\overline{EA}$ =

$\frac{EA}{(K \cdot R)^{2/3}(EI)^{1/3}}$ =1436.289793. It can be found until the occurrence of 7th contact the Eq. (4-4) ~ (4-6) are strictly followed but afterwards the deformation becomes diverged from expectations. This can be explained as with number of overlapped foldings increasing the whole structure becomes soft in vertical direction. In this direction every layer of folding has limited stiffness and the total stiffness decreases as more folds are connected in series because application of vertical force consumes larger displacement for more foldings than for fewer foldings as each layer folding consumes equal displacement for same load. Thus, the structure becomes softer along vertical direction. It acts as the substrate instead of a hard solid but as a soft foundation. Formation of overlapped foldings makes the lower part of structure function as a spring with limited stiffness which is decreased as more foldings formed. Upon the influence of vertical impact on the spring, spring is forced to vibrate at a frequency. As the downward impact meets with contact at the bounce back of the spring, large curvature forms to generate a larger moment. Whereas, when the downward impact meets with contact at the contraction of spring, the small curvature forms to generate a smaller moment. Therefore small and large irregular foldings can be found along the beam (Figure 15). Larger sized buckle takes longer time to self contact and results in lower force, on the contrary smaller sized one takes shorter time to self contact and results in higher force thus the output curves show divergences rather than straight plateau lines (Figure 14).

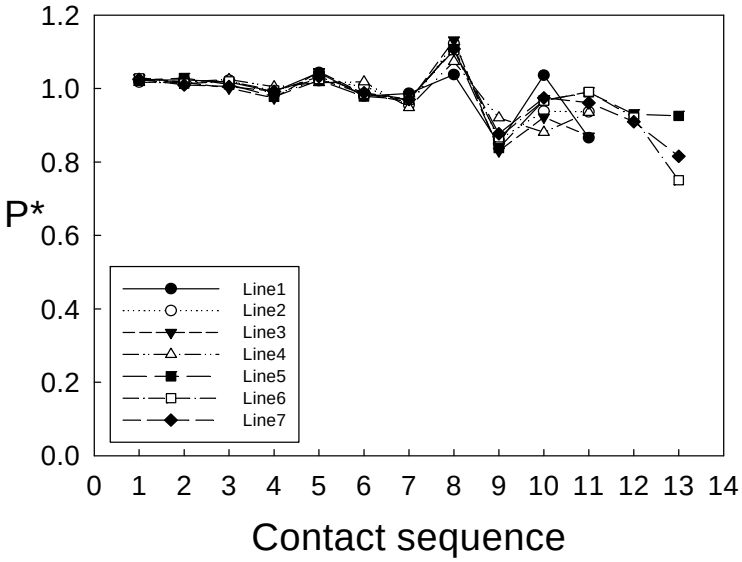
P*
Contact sequence
Line1
Line2
Line3
Line4
Line5
Line6
Line7

(a)

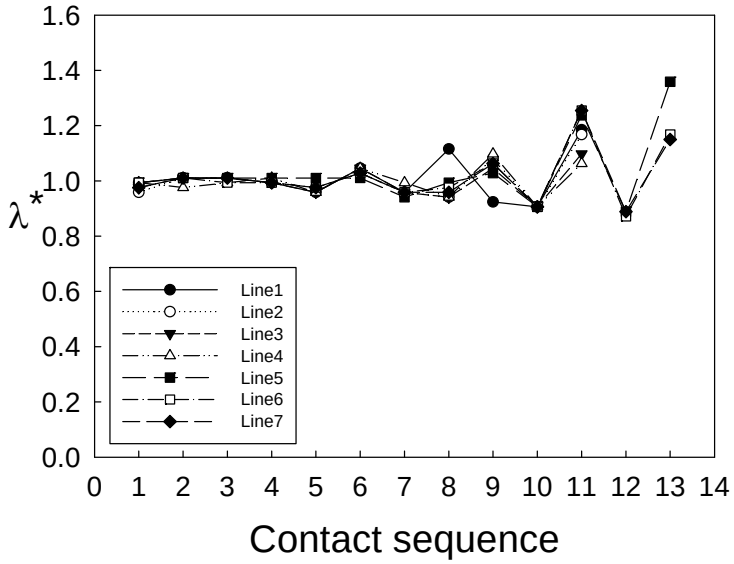
λ*
Contact sequence
Line1
Line2
Line3
Line4
Line5
Line6
Line7

(b)

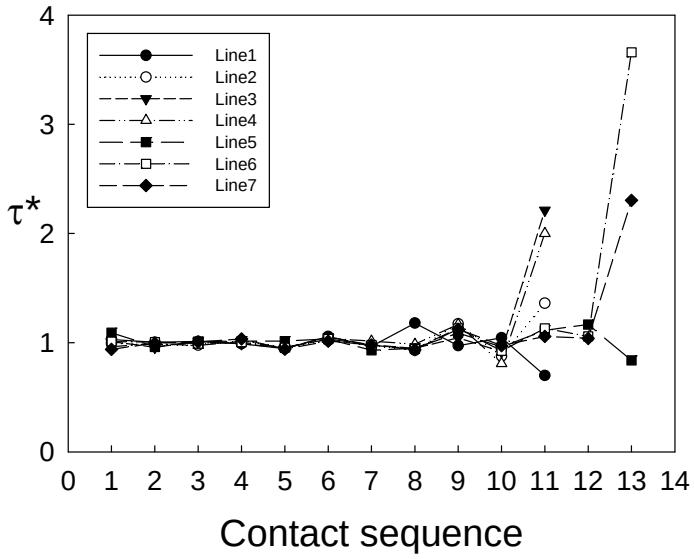

(c)

Figure 14 Simulation results with different beam total lengths. Line1 ~ Line7 represent the $\overline{H} = \frac{H}{(EI)^{1/3}(K\cdot R)^{-1/3}}$ =172.354775, 193.899122, 215.443469, 236.987816, 258.532163, 280.076510, 301.620857. $P^*=\frac{P'}{P}$, $\lambda^*=\frac{\lambda'}{\lambda}$, $\tau^*=\frac{\tau'}{\tau}$. P′, λ′, τ′ are directly measured from individual simulations. P, λ, τ are calculated from (4-4) ~ (4-6). (a) Normalized plateau load vs. contact sequence; (b) Normalized buckle wave length vs. contact sequence; (c) Normalized buckle forming rate vs. contact sequence.

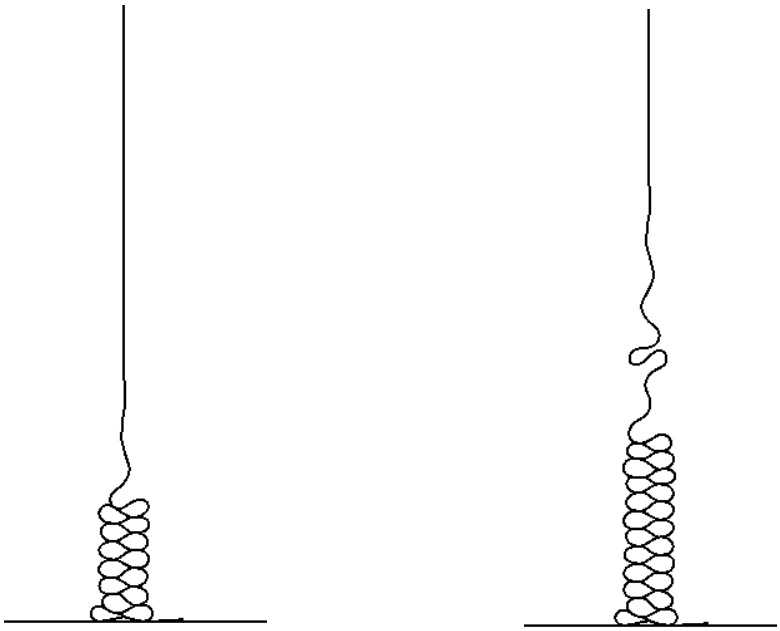

(a) (b)

Figure 15 Deformation of beam at different stages. (a) deformation with occurrence of fewer buckles; (b) deformation with occurrence of more buckles.

Cross section area elastic stiffness *EA* effect is discussed in the following. In Figure 16 parameters are used as: $\overline{EA} = \frac{EA}{(K\cdot R)^{2/3}(EI)^{1/3}}$ = 1679.894733, 2519.842100, 3359.789466, and 4199.736833; $\overline{H} = \frac{H}{(EI)^{1/3}(K\cdot R)^{-1/3}}$ = 125.992105; $\bar{h} = \frac{h}{(EI)^{1/3}(K\cdot R)^{-1/3}}$ =0.012599; $\overline{w} = \frac{w}{(EI)^{1/3}(K\cdot R)^{-1/3}}$ =1.259921. Cross section area elastic stiffness can affect the buckle shape. Area stiffness EA defines the capability of resisting the axial deformation. At relatively lower value of area stiffness EA deformation occurs both in bending direction and along axial direction. Thus the lower value EA results that the beam does not strictly follow Euler pure bending theory, and simultaneous significant axial deformation can occur. Usually the large portion of deformation is

consumed by the bottom heavily bent part, but low EA value results in the higher amount of axial deformation on the upper part beam. Bending and axial deformation co-evolves. As long as the global beam shape matches the wave length regulated by viscous force the uniform buckle will form (Figure 17).

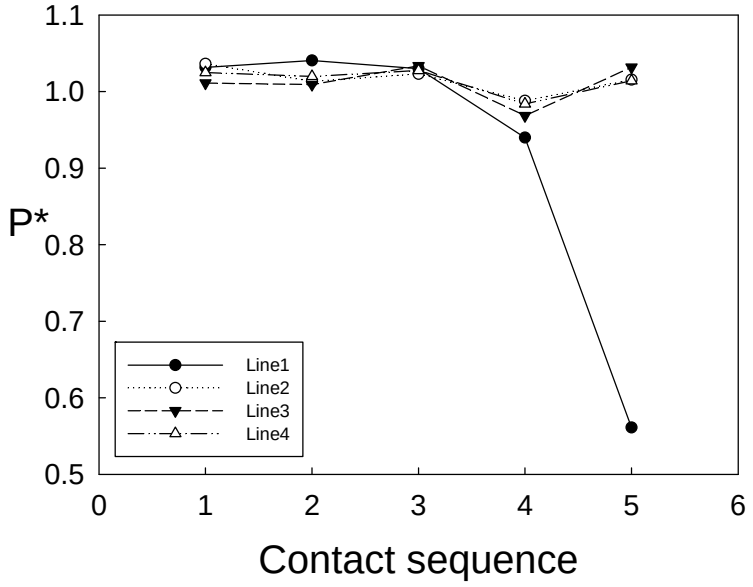

(a)

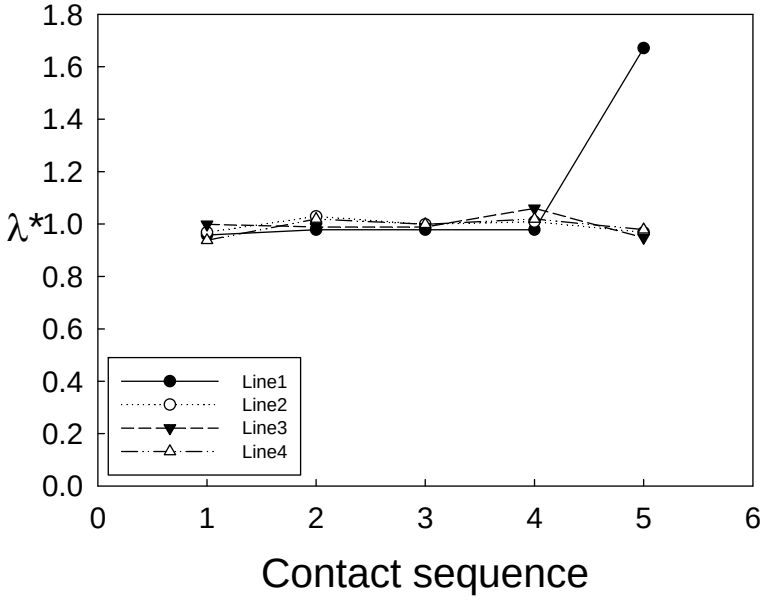

(b)

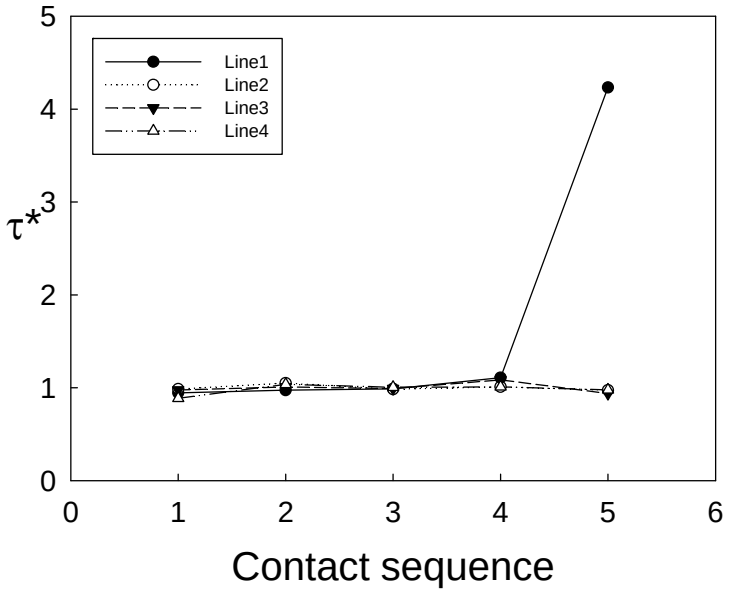

(c)

Figure 16 Simulation results with different beam axial stiffness. Line1 ~ Line4 represent the $\overline{EA} = \frac{EA}{(K \cdot R)^{2/3}(EI)^{1/3}} =$ 1679.894733, 2519.842100, 3359.789466, 4199.736833. $P^* = \frac{P'}{P}$, $\lambda^* = \frac{\lambda'}{\lambda}$, $\tau^* = \frac{\tau'}{\tau}$. P′, λ′, τ′ are directly measured from individual simulations. P, λ, τ are calculated from (4-4) ~ (4-6). (a) Normalized plateau load vs. contact sequence; (b) Normalized buckle wave length vs. contact sequence; (c) Normalized buckle forming rate vs. contact sequence.

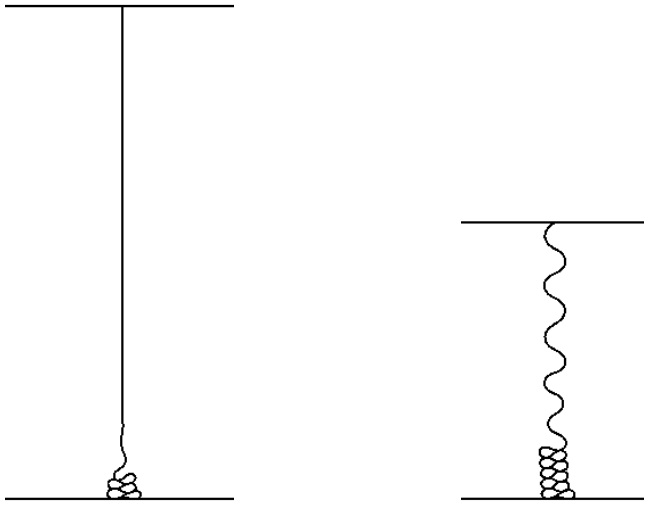

(a) (b)

Figure 17 Deformation of beam at different steps of compression $\overline{EA} = \frac{EA}{(K\cdot R)^{2/3}(EI)^{1/3}}$ =1679.894733. (a) earlier steps of compression with fewer buckles; (b) later steps of compression with more buckles.

Natural wave length *w* effect is discussed in the following. In Figure 18 $\overline{w} = \frac{w}{(EI)^{1/3}(K\cdot R)^{-1/3}}$ =2.519842, 5.039684, 6.299605, 10.079368, 12.599210, 25.198421, 31.498026; $\overline{H} = \frac{H}{(EI)^{1/3}(K\cdot R)^{-1/3}} = 125.992105$; $\overline{h} = \frac{h}{(EI)^{1/3}(K\cdot R)^{-1/3}} = 0.012599$; $\overline{EA} = \frac{EA}{(K\cdot R)^{2/3}(EI)^{1/3}} =$ 4199.736833. Natural wave length can regulate the buckle shape to some extent depending on how close is between natural wave length and viscous force resulted bending wave length. As natural wave length equals to the buckle wave length the bean will form the uniform buckles throughout the whole length as shown in Figure 19. w and λ are natural wave length and buckle wave length.

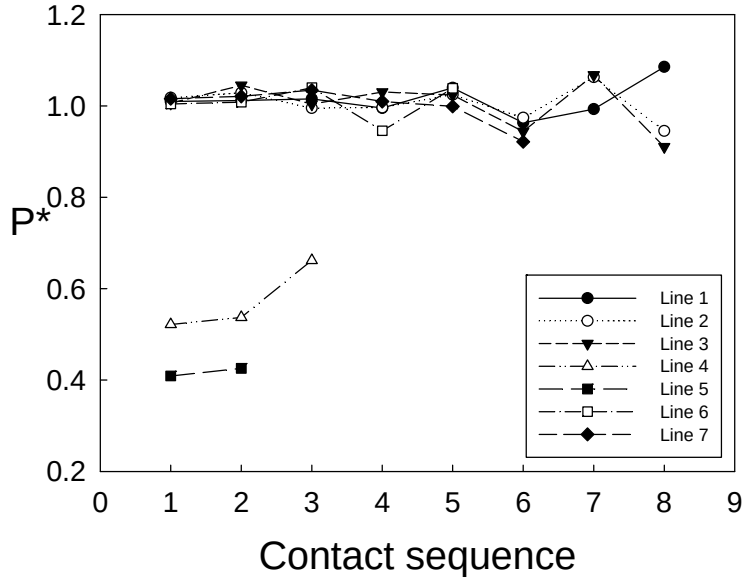
1.2
1.0
0.8
0.6
0.4
0.2
P*
0
1
2
3
4
5
6
7
8
9
Contact sequence
Line 1
Line 2
Line 3
Line 4
Line 5
Line 6
Line 7

(a)

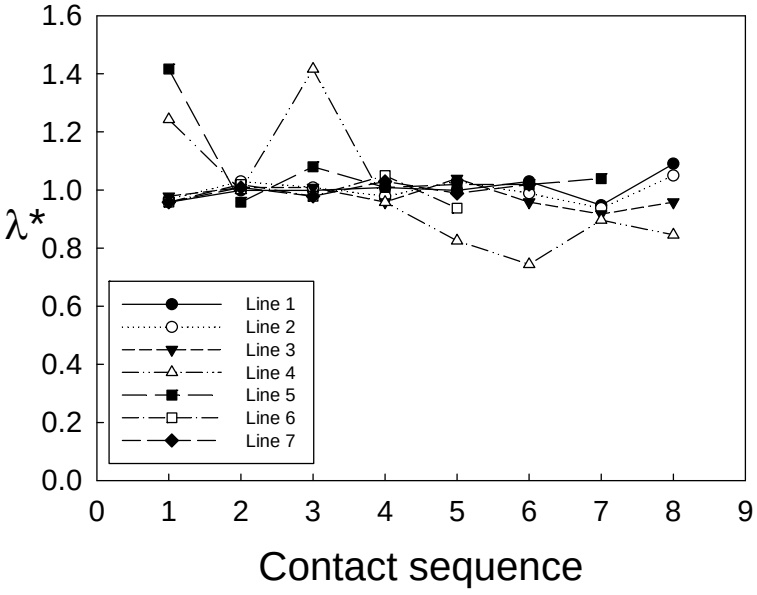
1.6
1.4
1.2
1.0
0.8
0.6
0.4
0.2
0.0
λ*
0
1
2
3
4
5
6
7
8
9
Contact sequence
Line 1
Line 2
Line 3
Line 4
Line 5
Line 6
Line 7

(b)

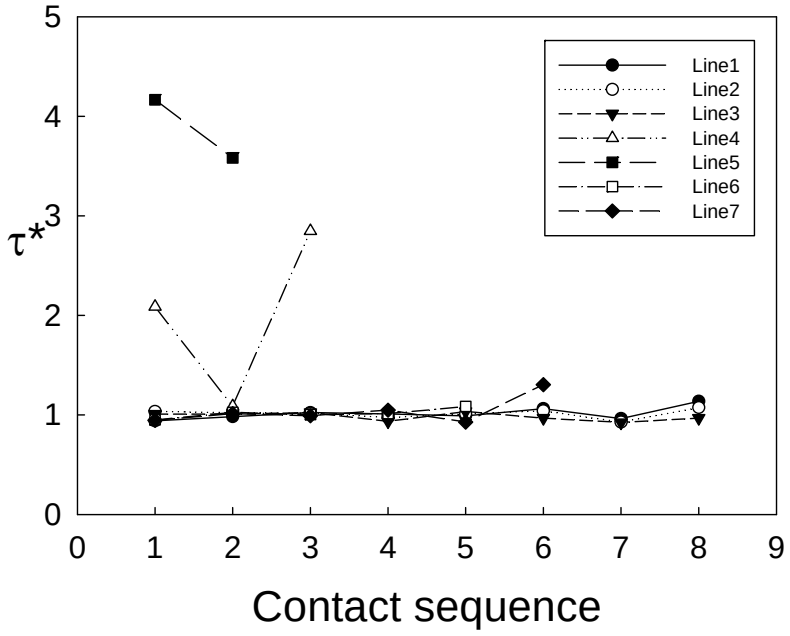

(c)

Figure 18 Simulation results with different beam natural wave lengths. Line 1 ~ Line 7 represent $\bar{w} = \frac{w}{(EI)^{1/3}(K\cdot R)^{-1/3}}$ =2.519842, 5.039684, 6.299605, 10.079368, 12.599210, 25.198421, 31.498026; Line 1 ~ Line 7 represent $\hat{w}=\frac{w}{\lambda}$ =0.203803, 0.407606, 0.509508, 0.815212, 1.019016, 2.038031, 2.547539. $P^*=\frac{P'}{P}$, $\lambda^*=\frac{\lambda'}{\lambda}$, $\tau^*=\frac{\tau'}{\tau}$. P′, λ′, τ′ are directly measured from individual simulations. P, λ, τ are calculated from (4-4) ~ (4-6). (a) Normalized plateau load vs. contact sequence; (b) Normalized buckle wave length vs. contact sequence; (c) Normalized buckle forming rate vs. contact sequence.

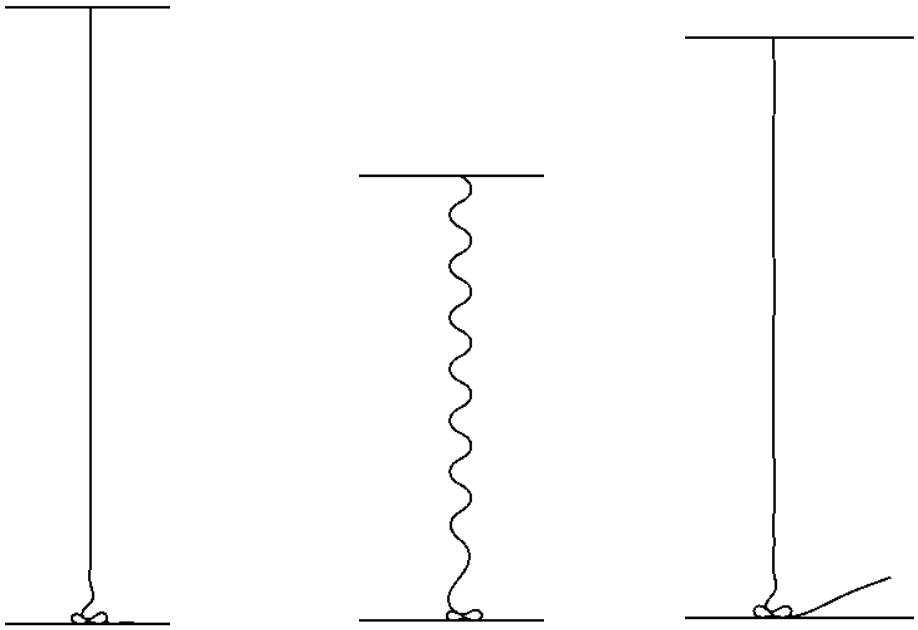

(a) (b) (c)

Figure 19 Deformation of beams with different natural wave lengths. (a) $\overline{w} = \frac{w}{(EI)^{1/3}(K\cdot R)^{-1/3}}$ =2.519842, $\frac{w}{\lambda}$ =0.20380312; (b) $\overline{w} = \frac{w}{(EI)^{1/3}(K\cdot R)^{-1/3}}$ =12.599210, $\frac{w}{\lambda}$ =1.01901558; (c) $\overline{w} = \frac{w}{(EI)^{1/3}(K\cdot R)^{-1/3}}$ =31.498026, $\frac{w}{\lambda}$ =2.54753894.

Natural wave magnitude *h* effect is discussed in the following. In Figure 20 $\overline{h} = \frac{h}{(EI)^{1/3}(K\cdot R)^{-1/3}}$ = 0.251984, 0.377976, 0.503968; $\overline{H} = \frac{H}{(EI)^{1/3}(K\cdot R)^{-1/3}}$ = 125.992105; $\overline{w} = \frac{w}{(EI)^{1/3}(K\cdot R)^{-1/3}}$ = 1.259921; $\overline{EA} = \frac{EA}{(K\cdot R)^{2/3}(EI)^{1/3}}$ = 4199.736833. The natural wave magnitude *h* can regulate the deformation transition from global buckle to local buckle. As deformation follows global buckle the formulas (4-4) ~ (4-6) are accurately observed, by contrast as local buckle is followed most deformation is consumed by initial natural wave shape and formulas

(4-4) ~ (4-6) are not observed. Occurrence of deformation along natural wave shape with smaller magnitude *h* is unlikely because the limited lateral viscous force cannot generate enough moment to resist the beam internal moment. Thus buckle folding of size greater than natural *h* should be followed (Figure 21 a). When magnitude *h/w* is large enough the whole structure is very soft along the height direction and becomes easy to collapse along the predefined natural wave shape. In fact it functions as a coil spring, and the global buckle shape regulated by lateral force should not be followed (Figure 21 b).

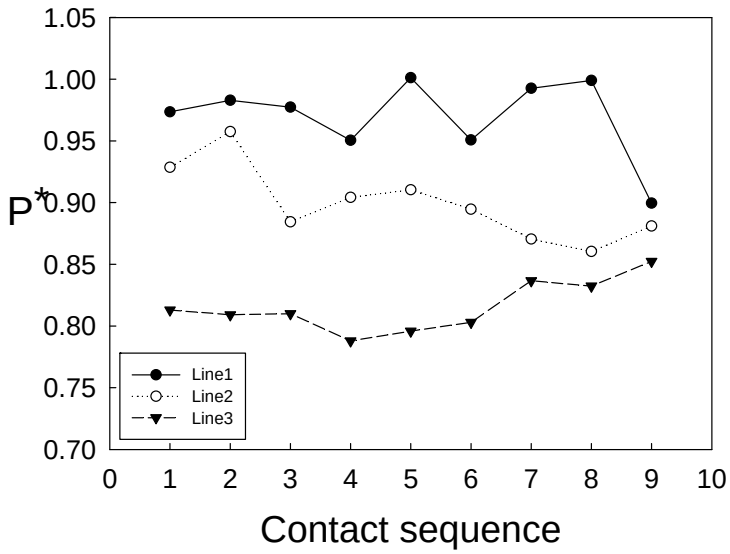

(a)

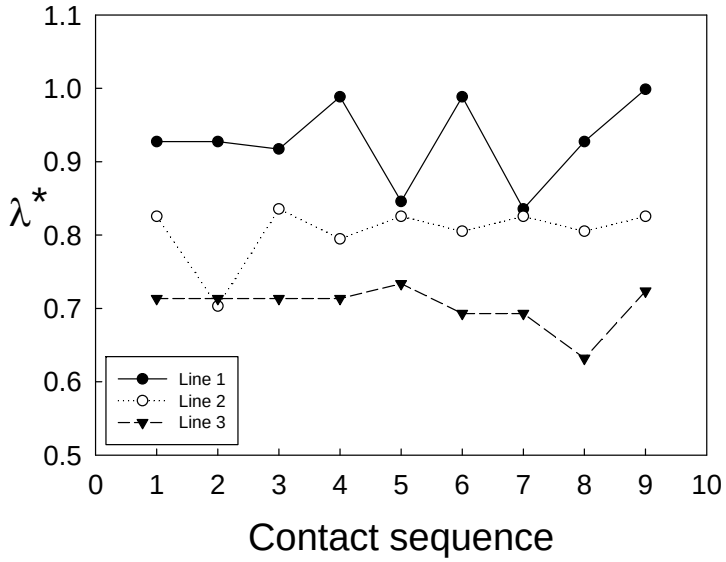

(b)

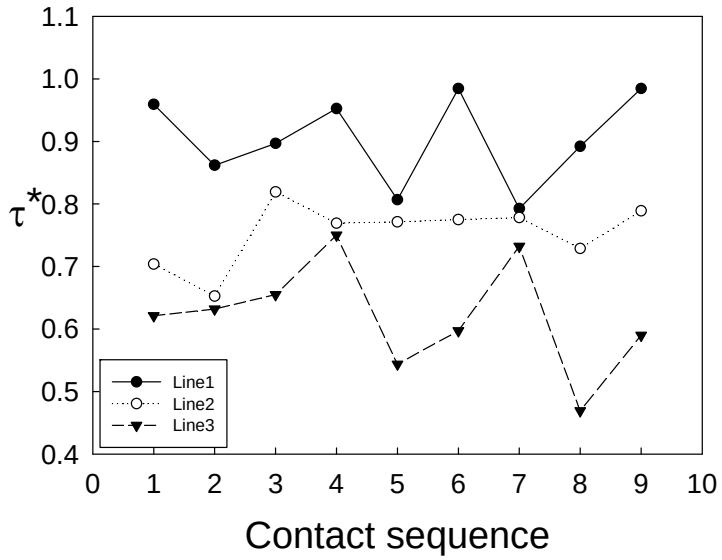

(c)

Figure 20 Simulation results with different beam natural wave magnitudes. Line1 ~ Line3 represent $\bar{h} = \frac{h}{(EI)^{1/3}(K \cdot R)^{-1/3}} =$ 0.251984, 0.377976, 0.503968; $P^* = \frac{P'}{P}$, $\lambda^* = \frac{\lambda'}{\lambda}$, $\tau^* = \frac{\tau'}{\tau}$. P′, λ′, τ′ are directly measured from individual simulations. P, λ, τ are calculated from (4-4) ~ (4-6). (a)

Normalized plateau load vs. contact sequence; (b) Normalized buckle wave length vs. contact sequence; (c) Normalized buckle forming rate vs. contact sequence.

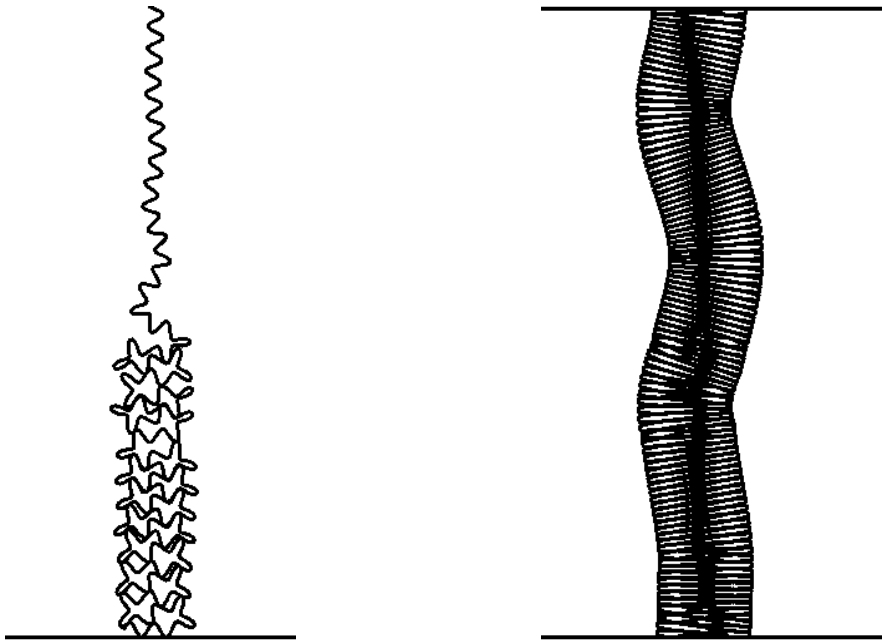

(a) (b)

Figure 21 Deformation of beams with different natural wave magnitudes. (a) $\bar{h} = \frac{h}{(EI)^{1/3}(K \cdot R)^{-1/3}}$ = 0.377976; (b) $\bar{h} = \frac{h}{(EI)^{1/3}(K \cdot R)^{-1/3}}$ = 1.259921.

Chapter 5 Conclusions

This work investigates the deformation mechanism of nanoturf subject to uniform compression and characterizes the nanoturf deformation by explicit formulas. The transverse relative movement induced friction with magnitude defined as proportional to the product of transverse velocity and the nanotube length projection on the rise direction acts as the confinement leading to the localized buckles. This is demonstrated by finite element simulation with single nanotube modeled as elastic Euler beam and friction modeled as the surface distributed viscous force. It is found that due to the unsymmetrical boundaries similar sized buckles evolve from bottom to the top end at stable buckle forming rate and compression buckle force. By taking advantage of dimensional analysis the size of buckle, buckle forming rate and compression buckle force can be expressed explicitly in terms of compression rate, bending stiffness and viscosity by matching the units of both sides in each formula. The structure geometric parameters and material properties at large ranges are expected to have notable effects on beam buckling. Their effects are discussed individually.

Several issues should be emphasized. First, the Eq. (4-4) ~ (4-6) are obtained from the displacement controlled loading condition. They are not applied to the force controlled or any arbitrary loading conditions, however, for which the individual finite element simulations can be established with the same structure properties as bending stiffness and viscosity. Second, apparently the material density of folded region is higher than that of regions filled with straight nanotubes thus the viscosity should be higher for the former region. But the lock of self folding resulted by vdW force leads to every buckle fold acting as solid support which does not have further significant deformation and influence on the successive buckle deformations. Third, by

using dimensional analysis to derive the Eq. (4-4) ~ (4-6) the nominal unit of length, time and force instead of the real units as meter, second and newton are used. The three coefficients are general values which are applied to all cases as long as each variable represents clear physical meaning.

References

[1] Suhr, J., Victor, P., Sreekala, L. C. S., Zhang, X., Nalamasu, O., and Ajayan, P. M., 2007, "Fatigue resistance of aligned carbon nanotube arrays under cyclic compression," Nat Nanotechnol, **2**(7), pp. 417-421.

[2] Zhang, Q., Zhao, M. Q., Liu, Y., Cao, A. Y., Qian, W. Z., Lu, Y. F., and Wei, F., 2009, "Energy-Absorbing Hybrid Composites Based on Alternate Carbon-Nanotube and Inorganic Layers," Adv Mater, **21**(28), pp. 2876-2880.

[3] Veedu, V. P., Cao, A. Y., Li, X. S., Ma, K. G., Soldano, C., Kar, S., Ajayan, P. M., and Ghasemi-Nejhad, M. N., 2006, "Multifunctional composites using reinforced laminae with carbon-nanotube forests," Nat Mater, **5**(6), pp. 457-462.

[4] Li, X. S., Zhu, G. Y., Dordick, J. S., and Ajayan, P. M., 2007, "Compression-modulated tunable-pore carbon-nanotube membrane filters," Small, **3**(4), pp. 595-599.

[5] Daraio, C., Nesterenko, V. F., and Jin, S. H., 2004, "Highly nonlinear contact interaction and dynamic energy dissipation by forest of carbon nanotubes," Appl Phys Lett, **85**(23), pp. 5724-5726.

[6] Teo, E. H. T., Yung, W. K. P., Chua, D. H. C., and Tay, B. K., 2007, "A carbon nanomattress: A new nanosystem with intrinsic, tunable, damping properties," Adv Mater, **19**(19), pp. 2941-2945.

[7] Cao, A. Y., Dickrell, P. L., Sawyer, W. G., Ghasemi-Nejhad, M. N., and Ajayan, P. M., 2005, "Super-compressible foamlike carbon nanotube films," Science, **310**(5752), pp. 1307-1310.

[8] Timoshenko, S., 1961, Theory of elastic stability, McGraw-Hill, New York,.

[9] Hutchens, S. B., Hall, L. J., and Greer, J. R., 2010, "In situ Mechanical Testing Reveals Periodic Buckle Nucleation and Propagation in Carbon Nanotube Bundles," Adv Funct Mater, **20**(14), pp. 2338-2346.

[10] Ge, L. H., Ci, L. J., Goyal, A., Shi, R., Mahadevan, L., Ajayan, P. M., and Dhinojwala, A., 2010, "Cooperative Adhesion and Friction of Compliant Nanohairs," Nano Lett, **10**(11), pp. 4509-4513.

[11] Yakobson, B. I., Brabec, C. J., and Bernholc, J., 1996, "Nanomechanics of carbon tubes: Instabilities beyond linear response," Phys Rev Lett, **76**(14), pp. 2511-2514.

[12] Liu, L., Cao, G. X., and Chen, X., 2008, "Mechanisms of nanoindentation on multiwalled carbon nanotube and nanotube cluster," J Nanomater, Article ID 271763, p. 12 pages.

[13] Misra, A., Greer, J. R., and Daraio, C., 2009, "Strain Rate Effects in the Mechanical Response of Polymer-Anchored Carbon Nanotube Foams," Adv Mater, **21**(3), pp. 334-338.

[14] Pathak, S., Cambaz, Z. G., Kalidindi, S. R., Swadener, J. G., and Gogotsi, Y., 2009, "Viscoelasticity and high buckling stress of dense carbon nanotube brushes," Carbon, **47**(8), pp. 1969-1976.

[15] Zhang, Q., Lu, Y. C., Du, F., Dai, L., Baur, J., and Foster, D. C., 2010, "Viscoelastic creep of vertically aligned carbon nanotubes," J Phys D Appl Phys, **43**(31), Article ID 315401, p. 7 pages.

[16] Tong, T., Zhao, Y., Delzeit, L., Kashani, A., Meyyappan, M., and Majumdar, A., 2008, "Height independent compressive modulus of vertically aligned carbon nanotube arrays," Nano Lett, **8**(2), pp. 511-515.

[17] Zbib, A. A., Mesarovic, S. D., Lilleodden, E. T., McClain, D., Jiao, J., and Bahr, D. F., 2008, "The coordinated buckling of carbon nanotube turfs under uniform compression," Nanotechnology, **19**(17), Article ID 175704, p. 7 pages.

[18] Fraternali, F., Blesgen, T., Amendola, A., and Daraio, C., 2011, "Multiscale mass-spring models of carbon nanotube foams," J Mech Phys Solids, **59**(1), pp. 89-102.

[19] Zhang, Y. Y., Zou, G. F., Doorn, S. K., Htoon, H., Stan, L., Hawley, M. E., Sheehan, C. J., Zhu, Y. T., and Jia, Q. X., 2009, "Tailoring the Morphology of Carbon Nanotube Arrays: From Spinnable Forests to Undulating Foams," Acs Nano, **3**(8), pp. 2157-2162.

[20] Yin, A. J., Chik, H., and Xu, J., 2004, "Postgrowth processing of carbon nanotube arrays - Enabling new functionalities and applications," Ieee T Nanotechnol, **3**(1), pp. 147-151.

[21] Cao, C. H., Reiner, A., Chung, C. H., Chang, S. H., Kao, I., and Kukta, R. V., Korach, C. S., 2011, "Buckling initiation and displacement dependence in compression of vertically aligned carbon nanotube arrays," Carbon, **49**(10), pp. 3190-3199.

[22] Dassault Systemes, 2009, ABAQUS Theory Manual (version 6.9)

[23] Zhou, W., Huang, Y., Liu, B., Hwang, K. C., Zuo, J. M., Buehler, M. J., and Gao, H., 2007, "Self-folding of single- and multiwall carbon nanotubes," Appl Phys Lett, **90**(7), Article ID 073107, p. 3 pages.